

The spectral state transition of Mkn 590, a potential link between AGNs and X-ray binaries?

B. Palit^{1*}, A. Różańska¹, A. G. Markowitz¹, D. Lawther², M. Vestergaard^{2,3}, J. J. Ruan⁴, T. Saha⁵, G. Walsh², A. Borkar⁶, M. Sniegowska⁶, K.-X. Lu⁷

¹Nicolaus Copernicus Astronomical Center, Polish Academy of Sciences, Bartycka 18, 00716 Warsaw, Poland.

²DARK, Niels Bohr Institute, University of Copenhagen, Jagtvej 155, 2200 Copenhagen, Denmark.

³Steward Observatory and Department of Astronomy, University of Arizona, 933 N. Cherry Avenue, 85721 Tucson, AZ, USA.

⁴Department of Physics & Astronomy, Bishop's University, 2600 rue College, Sherbrooke, J1M 1Z7 Québec, Canada.

⁵Inter-University Centre for Astronomy and Astrophysics (IUCAA), SPPU Campus, 411007 Pune, India.

⁶Astronomical Institute of the Czech Academy of Sciences, Boční II 1401, CZ-14100 Prague, Czechia.

⁷Yunnan Observatories, Chinese Academy of Sciences, Kunming, 650011, People's Republic of China.

*Corresponding author(s). E-mail(s): bpalit@camk.edu.pl;

Abstract

The Seyfert galaxy Markarian 590 offers a rare glimpse into the dynamic life cycle of black hole accretion, captured across multiple wavelengths from the years 1975 to 2025. Using the decade-long multi-band observations from the *Swift* observatory, we capture a clear spectral state transition analogous to those seen in X-ray binaries, but seldom observed in a single AGN. We track a complete AGN state transition in real time, as the source evolves from a faint, hard X-ray state to a bright, UV- and soft X-ray dominated phase. The X-ray loudness parameter α_{ox} follows a pronounced ‘V’-shaped dependence on Eddington ratio λ_{Edd} , with a break at $\lambda_{\text{Edd}} = 0.021 \pm 0.008$, coinciding with thresholds identified in population studies of changing-look quasars and X-ray binaries. Across this transition, Mkn 590 evolves through distinct accretion regimes in the Hardness Intensity Diagrams (HID): faint, flaring, transitional, and bright, on a timescale of ~ 10 years, which is well below classical viscous timescales for a geometrically-thin disk, but in agreement with the propagation of thermal wavefronts in the inner disk. When placed on the Fundamental Plane of black hole activity, the source broadly follows the expected radio/X-ray mass scaling, though with a 70% flatter slope, pointing towards a persistent coronal-jet coupling even in radiatively efficient states. Together, our results establish Mkn 590 as a rare, time resolved case of AGN state transitions and offer compelling evidence for scale-invariant accretion physics across the black hole mass spectrum.

1 Introduction

One of the most compelling issues in accretion of matter around compact objects is whether the nature of accretion flow is universal across the full range of black hole mass (M_{BH}) from tens to billions

of solar masses. Although M_{BH} spans more than eight orders of magnitude, covering a multitude of different type of objects such as black hole X-ray binaries (XRBs), intermediate mass black holes (IMBHs) and supermassive black holes (SMBHs) at the centers of active galactic nuclei (AGN), the broadband spectral energy distribution (SED) frequently shows multiple emission components that are common across multiple object classes.

A common component of the broadband spectrum in accreting black hole systems is typically attributed to the thermal emission from an optically-thick, geometrically-thin accretion disk. This emission is well described by a multi-color blackbody spectrum, where the peak flux scales with the disk temperature, which itself is inversely proportional to the black hole mass [1]. In XRBs, a relatively higher disk temperature ($\sim 10^7$ K) causes the thermal peak to shift into the soft X-ray regime (~ 1 keV). In contrast, SMBHs have cooler disks ($\sim 10^5$ K), leading the thermal emission to peak in the extreme ultraviolet (EUV) band. The second component occurs in hard X-rays, consisting of a high-energy tail beyond the disk spectrum and is not explained by standard models of accretion flows. It is commonly associated with an inverse Compton scattering of lower energy photons by a hot (10^{8-9} K), optically-thin plasma, known as the hot corona [2]. A third, distinct spectral feature frequently observed in AGNs is the soft X-ray excess (SXE), which appears at energies below 2 keV, and is detected in approximately 50% of low-redshift quasars [3]. This component is typically attributed to the presence of a warm corona [4, 5] situated at the intersection of the geometrically-thin accretion disk and the hot corona. However, in contrast to the hot corona, the warm corona is optically thick in nature and dominates the emission in the far-UV to soft X-ray band. Thus, in terms of energetics, this component may be interpreted as an extension or modification of the thermal disk emission. This effect is particularly relevant in hot disks of XRBs, where the SXE overlaps spectrally with the thermal disk emission. However, as discussed by [6], presence of such a warm Comptonizing layer in XRBs lead to systematically lower inferred black hole spin values, bringing them into closer agreement with those detected in black hole merger events by gravitational waves [7]. If the overall SED shape of accreting compact objects can indeed be explained by using only these few physical components, then as the accretion regime changes with time, one would expect a consistent pattern of variability across XRBs, IMBHs, and AGNs, reflecting the complicated interplay between the disk, the hot corona, and the warm corona.

XRBs are well known to undergo spectral state transitions, where the accretion flow switches from a high/soft state (dominated by thermal emission from the disk) to a low/hard state (dominated by Comptonized emission from the corona) and vice versa. Typically, a high/soft state is observed at higher mass accretion rates where the inner flow is similar to a standard Shakura-Sunayev disk. As the mass accretion rate drops by 2–3 orders of magnitude, the inner flow collapses into an optically-thin, hot flow, probably through evaporation [8]. These accretion state transitions lead to substantial changes in the emergent X-ray spectrum and are often accompanied by rapid outbursts, during which the X-ray luminosity can vary by several orders of magnitude [[9, 10]; see reviews by [11, 12]]. A complete evolution between the states is often visualized using hardness-intensity diagrams (HIDs), where the X-ray spectral hardness is compared against X-ray luminosity variations. These diagrams typically trace a characteristic ‘q’-shaped track over timescales of 2–4 years and specific regions signify distinct spectral states [13]. Attempts to identify similar state transitions in AGNs have been challenging, primarily due to their much longer accretion timescales. So far, only weak indications of the ‘q’-shaped track were recovered for large samples studies involving AGNs [14–17]. In order to robustly address this issue, the X-ray loudness parameter, α_{ox} , has been introduced as a proxy for comparing the coronal X-rays against the thermal disk UV luminosities in quasars [18–20] and bright AGNs [21, 22]. Interestingly, predictions based on the spectral state transitions in XRBs suggest that α_{ox} must exhibit a distinct ‘V’-shaped dependence on AGN luminosity or Eddington ratio, and thus has been proposed as a potential indicator of analogous spectral state transitions in AGNs [23].

Since the last decade, thanks to multiple repeated spectroscopic surveys like SDSS [Sloan Digital Sky Survey 24, 25], and to large-area time-domain photometric surveys such as the Zwicky Transient Facility [26], ATLAS [27], and eROSITA [28], a new type of highly variable AGNs has been discovered, called changing-look AGN (CLAGN) [29, and references therein]. For the first time, on human observational timescales, we can witness AGNs undergoing dramatic changes in luminosity, accompanied by the appearance/disappearance of the broad emission lines in the optical regime, originating from the broad line region (BLR) [first reported in Mrk 6 by 30]. To date, nearly 1000 CLAGNs have been identified, exhibiting transitions from Seyfert (Sy) Types 2, 1.9, 1.8, and 1.5 [AGN optical spectral subtypes defined by 31, 32] to Types 1 and 1.2 on timescales ranging from a few months to decades or longer [33, 34]. Thus, the study of these transient AGN is crucial for understanding the

physics of accretion onto SMBHs, as the CL event often challenges the standard inclination-based definition of the unified model of Seyfert galaxies [35]. In the majority of CLAGN, spectral and luminosity changes are driven by intrinsic variations in the accretion flow rate onto the SMBH [36–38], resulting in structural changes of the inner accretion flow and/or major variations in the net ionizing radiation that illuminates the BLR [36]. This breakthrough has renewed interests to test α_{ox} -based predictions and capture a state transition in accreting SMBHs, as CL events have been proposed as potential AGN analog(s) of state transitions observed in XRBs [39]. While sparse CLAGN samples have shown partial recovery of the characteristic ‘V’-shaped α_{ox} trend, clear evidence of full spectral state cycles remains rare. Other notable individual cases such as NGC 1566 [40], Mrk 1018 [41], NGC 2617 and ZTF18aajupnt [42] provide preliminary evidence, but comprehensive observational confirmation of state transition in individual AGNs are still lacking.

XRBs are known to host compact, steady radio jets, typically associated with the canonical low/hard and intermediate/hard states, and are quenched at the high/soft state, where the emission becomes dominated by the standard thin disk [43]. In the AGN context, Seyfert galaxies provide a compelling testbed for this analogy. Seyfert type-2 galaxies are observed to have systematically higher radio luminosities than their type-1 counterparts [44], and often display harder, power-law-dominated X-ray spectra indicative of a radiatively inefficient or truncated inner disk structure contrasting with the thermal disk-dominated spectra typically found in bright Seyfert type-1 galaxies [15]. These differences suggest a connection between accretion geometry and jet production, analogous to spectral state dependent jet behavior observed in XRBs. Recent high-resolution radio studies have further challenged the dichotomy between radio-loud and radio-quiet AGN. Even optically bright Seyfert galaxies have been shown to host compact, low-power, or unresolved jets [45], reinforcing the relevance of the AGN/XRB analogy beyond classical radio-loud systems. This has an implication for interpreting the radio behavior of CLAGN, where transitions in accretion state may trigger corresponding changes in the jet activity.

In this paper, we present the recently reactivated CLAGN Markarian 590 (hereafter Mkn 590) [38], which, as we demonstrate below, exhibits clear evidence of spectral state transition, analogous to those observed in XRBs. Earlier, such a result was obtained only for the case of the CLAGN Mrk 1018 [46], albeit with sparsely sampled data. Here, using optical/UV/X-ray data collected over the years by the *Neil Gehrels Swift Observatory*, we aim to determine the evolution of α_{ox} with Eddington ratio (λ_{Edd}). Our analysis reveals a critical accretion rate at a few percent of the Eddington luminosity at which the state transition appears to occur, in agreement with estimates in the literature for other black hole systems [23, 47]. It should be noted that the evolution of the BLR structure as a function of luminosity was suspected independently of CL events [e.g. 48], and it is extremely important to investigate this issue in parallel with our present work. However, this requires detailed spectroscopic analysis, and we address this topic in a separate publication.

We also examine the complex interplay between hot/warm corona and thermal disk in Mkn 590, by attempting to construct non-standard HIDs, in which we observe a clear separation between the low/hard (faint) and high/soft (bright) spectral states. Additionally, by compiling archival, quasi-simultaneous radio and X-ray observations, we place Mkn 590 on the Fundamental Plane (FP) of black hole activity [49], suggesting a possible link between the accretion state and the jetted activity in this source.

The structure of the paper is as follows: Sec. 2 presents the past and present view of Mkn 590, especially how the source changed its Seyfert activity type over the past decades. The data used in this paper are described in Sec. 2.1, 2.2 and Appendix A. Parametrization of spectral state transition is established in details in Sec. 3, while the Sec. 4–6 present results on α_{ox} , the HID, and the fundamental plane, respectively. The summary and conclusions are provided in Sec. 7.

2 Our laboratory: Mkn 590

Mkn 590 ($z = 0.0264$), located in the direction of the constellation Cetus, stands out as one of the most important nearby CLAGN, having exhibited multiple CL events over the past five decades. Since the last decade, it has been continuously monitored using some of the most advanced ground and space-based observatories. An overall historical activity of Mkn 590 is displayed in Fig. 1.

A compilation of optical, UV, and X-ray observations spanning from 1970 to 2015 reveals at least two major CL events: first, there was a brightening or ‘turn-on’ phase between 1973 and 1989. During the early 1970s, optical observations from the Lick Observatory classified Mkn 590 as a Sy 1.5 within the AGN unified scheme [50, 51], characterized by relatively modest but detectable broad $\text{H}\beta$

emission. Subsequent observing campaigns, using the 1.8 m Perkins telescope at Lowell Observatory, indicate the 5100Å continuum luminosity increasing by a factor of ~ 16 through the early 1980s up to the early 1990s, while the broad H β component underwent significant strengthening in flux, marking a clear transition to a Sy 1 activity state [52]. As shown in Fig. 1 using green and blue markers, this period was also characterized by the increased emission in UV and X-rays as observed by some of the earliest high energy missions – the *International Ultraviolet Explorer* (IUE), the *European X-ray Observatory Satellite* (EXOSAT) and the *ROentgen SATellite* (ROSAT). The 1450Å UV continuum and 2–10 keV integrated hard X-ray emission increased by factors of ~ 5 and 2 respectively, thus showing a near-simultaneous response across multiple wavebands [53, 54].

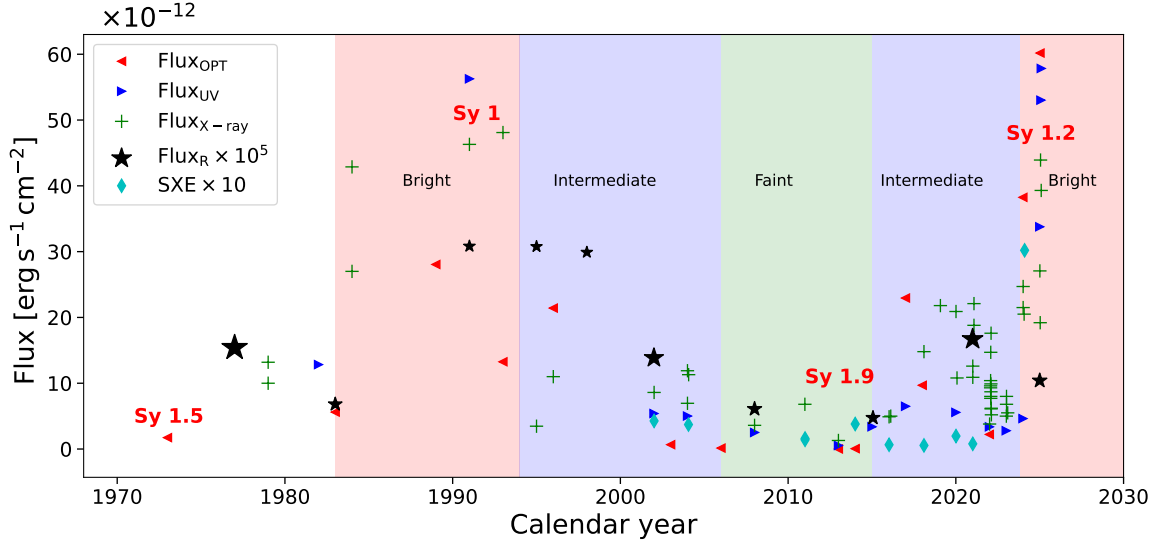


Fig. 1 Guideline multi-wavelength light curve of Mkn 590 compiled from various facilities between 1970 and 2025, also presented in [55, 56]. Details on data collection are described in Appendix A and listed in Tab. 2. In the case of optical/UV/radio measurements we present monochromatic fluxes, while in case of X-rays, the model dependent fluxes integrated over 2–10 keV are shown. The SXE and radio fluxes are offset vertically for clear comparison with other bands. The marker size of radio data scales with the beam size of radio facility. Three major CL events in the late 1980s, in the 2000s, and starting late 2023 are clearly depicted. The radio peak delay during the early 1990s is further discussed in Sec 2. the bright, intermediate, and faint activity level are shaded and defined empirically based on X-ray flux level and are intended for interpretive purposes only.

Then, from the late 1990s through the 2010s, the source entered a shutdown phase, during which the luminosity across all wavebands underwent a steady decline [55, hereafter D14]. A 2003 SDSS optical spectrum shows only a weak broad H β component; by then, the optical continuum had dropped by an order of magnitude. Meanwhile, X-ray observations with *XMM-Newton* and *Chandra* tracked a drop in X-ray flux by a factor of ~ 10 from the early 1990s to 2004 [57]. By 2014, Mkn 590 had reached a historic low state, with X-ray and optical fluxes reduced by ~ 2 orders of magnitude relative to its peak phase in the 1990s, while the optical spectral type had transitioned to Sy 1.8-1.9, marking a second CL transition. Despite this extreme low state, evidence for the persistence of the BLR was found via UV spectroscopy, which shows a continued presence of the Mg II $\lambda\lambda 2796, 2803$ emission lines [58], while optical spectroscopy obtained during 2017–2018 with VLT/MUSE and Subaru/HDS reports weak but significant broad Balmer lines [59, 60]. These observations suggest that the BLR in Mkn 590 remained largely intact even as the ionizing continuum weakened substantially.

Then, starting in 2017, Mkn 590 exhibited renewed flaring activity in the X-ray, UV, and optical bands on timescales of ~ 100 days since 2017, broadly consistent with the thermal timescales as expected from the standard accretion disk theory [see detailed light curve in 61]. This flaring subsided by the end of 2022, as the source momentarily lowered its UV/X-ray intensity.

This brief low-flux period ended in an abrupt and sustained spike in broadband fluxes post-2023, marking the second major re-brightening episode in fifty years. As tracked with *Swift*, the far-UV and X-ray fluxes increased by factors of ~ 12 and ~ 15 , respectively, from late 2023 through early 2025, the largest such increases in the last fifty years [38]. Timely optical spectroscopic observations taken in Nov. 2024 at Siding Spring Observatory confirms the reappearance of the broad H β component,

with its flux now six times stronger than in 2003, signaling a changing-look transition of Mkn 590 back to a Sy 1 activity type [38].

As illustrated by the cyan diamonds in Fig. 1, the SXE in Mkn 590, visible in the early 2000s, had completely disappeared by 2008–2011 [62, 63]. SXE flux measurements were obtained by fitting a distinct spectral component in the 0.2–2 keV band. A weak SXE emission component reappeared in 2014, suggesting the start of the episodic accretion activity observed in the years following [58]. Until 2021, Mkn 590 had not exhibited a full recovery of the SXE, with only a weak component detected [63]. However, the CL event of 2025 revealed the emergence of an independent, strong SXE component, likely associated with the warm corona and rising faster than the hard X-ray power-law emission [38].

Mkn 590 is also variable in the GHz regime, and has been monitored across three decades [56]. The earliest reported radio observation dates back to 1977, when the source was detected with the Westerbork Synthesis Radio Telescope (WSRT) at a flux density of 11 mJy in the 1.4 GHz band [64]. Over the following two decades, multiple arcsec-resolution observations with the Very Large Array (VLA) spanning frequencies from 1.4 to 8.4 GHz measure a mean flux density of ~ 4 mJy. After the turn of the century, the radio emission intensity starts to exhibit a gradual decline through 2015 where fresh VLA measurements recorded a historic low core radio flux density of 3 mJy [56]. This coincided with detection of a faint, radio jet at a flux density of ~ 1.7 mJy at 1.6 GHz using high-resolution sub-arcsec resolution measurements by the European VLBI Network (EVN) [65]. More recent observations with the Australian Square Kilometer Array Pathfinder (ASKAP) as part of the Variables and Slow Transients (VAST) survey from mid-2022 [66] and the Giant Meterwave Radio Telescope (GMRT) in early 2025 [67] reports a modest increase in GHz-band radio flux densities, reaching levels of up to ~ 5 mJy, and indicating an upward rising trend, tracking the contemporaneous brightening observed at other wavelengths and approaching flux levels last seen in the early 1980s. Interestingly, the 2015 radio measurements are consistent with the Fundamental Plane of black hole activity for sources in the low/hard state [49, 56].

From Fig. 1, it is evident that Mkn 590 has undergone multiple significant changes in flux across the optical, UV, and X-ray bands over the past five decades, indicating transitions between distinct accretion levels. We empirically define the boundaries between accretion levels from the observed intensity evolution, for epochs with X-ray fluxes exceeding 2×10^{-11} erg s $^{-1}$ cm $^{-2}$ in the 0.3–10 keV band classified as bright and below 1×10^{-11} erg s $^{-1}$ cm $^{-2}$ as faint. These different brightness epochs are shown as shaded regions in Fig. 1 and provide a phenomenological framework for interpreting the accompanying spectral evolution.

At present, Mkn 590 remains the subject of extensive multi-wavelength monitoring with a broad range of facilities, alongside ongoing theoretical modeling of its spectral and timing properties. These coordinated efforts aim to probe the structure and evolution of the inner accretion flow as it enters a new elevated accretion regime. Our current work concerns whether Mkn 590 undergoes spectral state transitions analogous to those seen in XRBs. All data and reduction procedures are described in two subsections below. For the purpose of our studies we adopt standard cosmological parameters: Hubble constant $H_0 = 69.6$ km s $^{-1}$ Mpc $^{-1}$, mass density $\Omega_m = 0.3$, and density of dark energy $\Omega_\lambda = 0.7$. In estimating the basic observable properties of Mkn 590, we always use a luminosity distance of $L_D = 115$ Mpc [68], and the mass of the central black hole $M_{\text{BH}} = 4.75 (\pm 0.74) \times 10^7 M_\odot$, which has been estimated based on extensive reverberation mapping campaigns [69].

2.1 The *Swift* data

In the last decade, the *Swift* satellite has achieved a total of 420 pointings of Mkn 590, with especially higher-cadence observations since 2017, when the source began to exhibit flaring activity. For the purpose of this study, we analyze observations obtained between December 10, 2013, and September 28, 2025, observed by two instruments onboard *Swift*, the X-Ray telescope (XRT; [70]) and UV/optical Telescope (UVOT; [71]). This dataset includes bi-weekly cadence observations previously published in the work by [61], conducted under *Swift* GO Cycle 14 (Programs 1417159 and 1417168; PI: Vestergaard), and joint *NuSTAR*-*Swift* observations from *NuSTAR* Cycle 5 (Program 5252; PI: Vestergaard). It also incorporates a period of high-cadence monitoring (every 1–2 days) from September 2017 to February 2018, obtained through *Swift* Cycle 13 Director’s Discretionary Time (PI: Vestergaard). The corresponding *Swift* target IDs include 37590, 80903, 88014, 94095, 10949, 11481, 11542, and 13172. We further include data presented by [72], covering the period from June 2021 to September 2024. These data were obtained through *Swift* Cycle 18 (Program 1821134;

PI: Lawther), a VLBA-*Swift* joint proposal (Program VLBA/22A-217; PI: Vestergaard), Swift Cycle 19 (Program 1922187; PI: Lawther), and another VLBA-*Swift* joint program (Program VLBA/24A-374; PI: Vestergaard). Additionally, we complemented our entire dataset with new *Swift* observations spanning from between October 2024 to September 2025 (obsIDs 97768014 to 98338027; Program 2124212 cycle 21, PI: Lawther; Program 2124218 cycle 21, PI: Walsh; Program VLBA/25A-323, VLBA/Swift, PI: Walsh).

We retrieved the XRT data products from the UK *Swift* Science Data Center ([73]). Each individual XRT spectrum was generated choosing a 30" circular extraction region centered on the source and a co-spatial background annular region of 35–75". The UVOT data across all six filters (V, B, U, UVW1, UVM2 and UVW2) were processed using HEASOFT v6.32 and the most recent calibration files. We performed aperture photometry using `uvotsource`, employing a 5" circular region on the source and a 35–75" co-spatial background annulus. This choice reduces photometric errors which might be arising due to point spread function instability during the orbital motion of the telescope [74]. In addition, we neglected observations affected by low sensitivity regions on the detector, resulting in abrupt flux drops [75].

We correct the flux densities in each filter for Galactic extinction using the standard dust maps [76]. The color excess at the source coordinates was obtained assuming an extinction law with $R = 3.1$ [77], and we apply extinction corrections at the effective wavelengths of the UVOT filters using the Python packages `sfdmap`¹ and `extinction sfdmap`². Finally, we subtract the host galaxy contribution for each filter adopting the methodology followed by [72].

Overall, we obtain 399 XRT, 365 UVOT V, B, U, UVW1, UVW2 and 151 UVM2 data points. The majority of these observations, up to early 2025, have been previously reported [38, 67, 72]. In our current work, we incorporate new data obtained through September 28, 2025, during which the average X-ray flux during the month of September 2025 remained elevated at $\sim 7.7 \times 10^{-11} \text{ erg s}^{-1} \text{ cm}^{-2}$ in the 0.3–10 keV band, as shown in Fig. 1.

2.2 Radio and X-ray data for the Fundamental Plane

Based on the historical data in Fig. 1 and Appendix A, we complied all the contemporaneous X-ray/radio data to explore the accretion-ejection similarities across black hole masses. As shown in Tab. 1, we identified seven epochs during which radio and X-ray observations were taken within one year, and which represent distinct activity states. We converted the radio flux densities measured at different frequencies to a common reference frequency of 5 GHz, ensuring consistency across epochs and facilitating comparison with established Fundamental Plane relation defined at this frequency. To minimize uncertainties arising from differing beam sizes, we restricted this sub-sample to observations with beam sizes of a few arcseconds only. The frequency conversion was performed assuming a standard radio spectral index and intrinsic 1σ scatter of $\alpha = -0.8 (\pm 0.2)$ [56, 78] typical for this source, such that the flux density scales with frequency as $S_\nu \propto \nu^\alpha$, yielding

$$S_{5 \text{ GHz}} = S_{1.4 \text{ GHz}} \left(\frac{\nu_{5 \text{ GHz}}}{\nu_{1.4 \text{ GHz}}} \right)^\alpha. \quad (1)$$

We obtained the X-ray fluxes prior to the year 2000 from the XMM-Newton upper-limit server³. For detections earlier than that from missions such as *EXOSAT* and *ROSAT*, which typically observed in the 0.2–2 keV band, we converted to the 2–10 keV band using the `WebPIMMS`⁴ tool, assuming a power-law continuum with a X-ray photon index of $\Gamma = 2$. Post year-2000, we used *Swift* observations by fitting the X-ray spectra in the 2–10 keV range and extracting the unabsorbed X-ray fluxes. We converted the radio and X-ray flux values to luminosities assuming standard cosmological parameters, and we present those values in Tab. 1.

3 Parametrization of spectral state transitions

We trace the spectral state transition of Mkn 590 by following the evolution of key AGN diagnostic parameters such as the X-ray loudness parameter α_{ox} , the Eddington fraction λ_{Edd} , the hardness

¹<https://github.com/kbarbary/sfdmap>

²<https://extinction.readthedocs.io/en/latest/index.html>

³<https://www.cosmos.esa.int/web/xmm-newton/uls-userguide>

⁴<https://heasarc.gsfc.nasa.gov/cgi-bin/Tools/w3pimms/w3pimms.pl>

Table 1 The simultaneous radio and X-ray fluxes used for constructing the Fundamental Plane of Mkn 590 as described in Sec. 2.2. The computed luminosities in the radio and X-rays are shown in columns 3 and 4, respectively, followed by their ratio given in column 5, and pre-defined activity level and representative year in column 6. No measurement errors were available for the ASKAP/VAST observation.

Radio facility 5 GHz flux density (mJy)	X-ray mission 2–10 keV Flux ($\times 10^{-11}$ erg s $^{-1}$ cm $^{-2}$)	$\log \left(\frac{\nu L_{\text{5 GHz}}}{\text{erg cm}^{-2}} \right)$	$\log \left(\frac{L_{\text{2–10 keV}}}{\text{erg cm}^{-2}} \right)$	$\log \left(\frac{\nu L_{\text{5 GHz}}}{L_{\text{2–10 keV}}} \right)$	Activity level Rep. Year
VLA-A 1.75 ± 0.49	<i>EXOSAT</i> 3.63 ± 0.11	38.14 ± 0.12	43.75 ± 0.01	-5.61	Bright 1984
VLA-A 5.55 ± 0.62	<i>ROSAT</i> 3.82 ± 0.09	38.40 ± 0.05	43.77 ± 0.01	-5.37	Bright 1991
MERLIN 4.16 ± 0.30	<i>ROSAT</i> 0.286 ± 0.01	38.52 ± 0.03	42.74 ± 0.01	-4.13	Intermediate 1995
VLA-A 1.57 ± 0.40	<i>Swift-XRT</i> 0.36 ± 0.03	38.09 ± 0.11	42.65 ± 0.04	-4.66	Faint 2008
VLA-A 1.15 ± 0.31	<i>Swift-XRT</i> 0.24 ± 0.05	37.96 ± 0.14	42.58 ± 0.08	-4.62	Faint 2015
VAST 4.03	<i>Swift-XRT</i> 1.10 ± 0.05	38.50	43.24 ± 0.02	-4.74	Intermediate 2021
GMRT 2.68 ± 0.69	<i>Swift-XRT</i> 2.54 ± 0.30	38.32 ± 0.12	43.60 ± 0.05	-5.28	Bright 2025

ratio HR , and the radio/X-ray scaling. In this section, we describe the methods used to estimate these quantities from the observational data.

The classical optical-to-X-ray spectral index for AGN and quasars is given by

$$\alpha_{\text{ox}} = -\frac{\log \left[L_{\text{2keV}} / L_{\text{2500\AA}} \right]}{2.605} \quad (2)$$

[19, 79], with 2500 Å and 2 keV emission as proxies for emission from the UV-emitting disk and the X-ray corona, respectively.

Since the re-brightening of Mrk 590 is accompanied by the detection of the SXE [38], usually observed below 2 keV, for the purpose of this paper, we define two new α_{ox} parameters, corresponding to the soft and the hard X-ray bands, which better trace the behavior of the warm and the hot coronae, respectively than the standard α_{ox} (Eq. 2):

$$\alpha_{\text{ox}}^{(0.5)} = -\frac{\log \left[L_{0.5\text{keV}} / L_{\text{2500\AA}} \right]}{2.003}, \quad (3)$$

$$\alpha_{\text{ox}}^{(4)} = -\frac{\log \left[L_{4\text{keV}} / L_{\text{2500\AA}} \right]}{2.906}, \quad (4)$$

For all three cases, we estimate the monochromatic luminosity at 2500 Å, after selecting only those *Swift*-UVOT observations with simultaneous UVW1 and UVW2 coverage. After subtracting the host galaxy contribution and correcting the photometric flux densities for Galactic extinction, as described in Sec. 2.1, we use a simple linear interpolation to estimate the flux density at 2500 Å and converted it into monochromatic luminosity.

Next, to derive monochromatic X-ray fluxes, we fit the *Swift*-XRT spectra using a pegged power-law model (`pegpwrlw`) in `XSPEC` [version 12.13.1; 80]. Unlike a simple power-law model, `pegpwrlw` normalizes the spectrum to the flux within a specified energy band rather than at a single pivot energy, allowing for a more direct and robust determination of band limited and monochromatic fluxes. For the monochromatic 0.5 keV fluxes, we fit over the 0.3–2 keV band only; for the 2 and 4 keV monochromatic fluxes, we fit over the 2–10 keV band. We then convert these monochromatic fluxes into monochromatic luminosities in units of erg s $^{-1}$ Hz $^{-1}$.

We parameterize Mkn 590’s highly variable accretion rate using the Eddington luminosity ratio denoted by λ_{Edd} , defined as the ratio of bolometric luminosity to Eddington luminosity, or $L_{\text{bol}} / L_{\text{Edd}}$. There are two main uncertainties associated with estimating λ_{Edd} , namely black hole mass, M_{BH} , and bolometric correction factor, K_{bol} , defined as the ratio of L_{bol} to X-ray luminosity L_{bol} . Several distinct formalisms have been developed so far to empirically estimate K_{bol} based on the relatively

stable accretion phases of AGN and quasars (for discussion see Appendix B.1). However, as shown in Fig. 1 and further demonstrated in this work, Mkn 590 has undergone dramatic accretion rate transitions, exhibiting strong variability in both the X-ray and optical/UV bands. As demonstrated in Appendix B.2, the choice of L_{bol} estimator significantly affects the inferred $\alpha_{\text{ox}}-\lambda_{\text{Edd}}$ relation. This motivates the use of a source-specific approach: directly integrating the intrinsic broadband SED over 0.001–50 keV (further detailed in Appendix B.1). We adopt this SED integration method for the primary scientific analysis in this work since it provides the most accurate measure of the intrinsic SED of the Mkn 590 nuclear emission.

Another widely used diagnostic for spectral states in X-ray studies of XRBs and ULXs is the X-ray hardness ratio (HR). It provides a model-independent measure of the X-ray spectral shape. We adopt the definition $HR = (H - S)/(H + S)$, where H and S are the 2–10 keV and 0.3–2 keV photon count rates, respectively. In XRBs, they represent the X-ray corona and the thermal disk emission respectively, hence, HR acts as a proxy for the corona versus the disk-dominated spectral states. In AGN, however, the accretion disk emits predominantly in the EUV rather than in soft X-rays, so in this case HR traces mainly changes within the hot/warm coronal components. We use $\alpha_{\text{ox}}^{(0.5)}$ and $\alpha_{\text{ox}}^{(4)}$ to track the ratio of the power between the disk and warm or hot coronae, respectively.

We propagated the 1σ uncertainties from UVOT photometry, X-ray spectral fitting, observed XRT count rates, and the reported errors in archival radio and X-ray measurements into the final uncertainties on the derived quantities α_{ox} , HR , and the radio-to-X-ray luminosity ratio. This was done by adding the relative errors of the individual measurements in quadrature. We followed the same strategy to estimate the uncertainties on λ_{Edd} .

4 The observed $\alpha_{\text{ox}}-\lambda_{\text{Edd}}$ relation

Here we discuss the evolution of α_{ox} as a function of λ_{Edd} in Mkn 590. This marks the most detailed measurement of α_{ox} in a single CLAGN across an entire CL event. The $\alpha_{\text{ox}} - \lambda_{\text{Edd}}$ trend is shown in the left panel of Fig 2, tracing a clear ‘V’-shape.

In order to determine the turnover point between the two arms in the ‘V’-shaped trend, we employed a piecewise linear regression in Python⁵ [81]. Details of this algorithm are given in Appendix C. The algorithm detects only one statistically significant break point at $\log \lambda_{\text{Edd}} = -1.67 \pm 0.04$ with a null hypothesis probability of $p = 10^{-58}$. The position of the break point is marked by a vertical, red, dashed line in Fig. 2, and the 95% confidence interval is indicated by a light red shaded region. Subsequently, we fitted the data on each side of this break point using the Deming regression, a statistical technique that accounts for measurement uncertainties in both variables and estimates the best fit line by minimizing the orthogonal (error-weighted) distances of the points from the regression model (see Appendix C for details). To estimate the confidence intervals for Deming regression, we performed 5000 bootstrap resamplings, deriving the 95% confidence regions shown as purple shaded bands in Fig. 2. The best fit linear models for the left and the right arms are $\alpha_{\text{ox}} = (-0.14 \pm 0.02) \log \lambda_{\text{Edd}} + (0.86 \pm 0.04)$ and $\alpha_{\text{ox}} = (0.18 \pm 0.05) \log \lambda_{\text{Edd}} + (1.40 \pm 0.06)$ respectively.

At about 2% of L_{bol} , the break point is comparable to the implied critical λ_{Edd} value constrained from sparsely sampled studies of CLAGN, CL quasars, and TDEs [36, 39, 47, 82–84]. A comparison with predictions from simulations for XRBs and with fading quasars is shown in Fig. 3. Despite differences in methodologies, the three populations appear to display a turnover in α_{ox} at 1–2% of L_{bol} , reinforcing the idea that a common structural transition in the inner accretion flow occurs near this critical threshold for accreting compact objects.

Next, we present the dependence of $\alpha_{\text{ox}}^{(0.5)}$ and $\alpha_{\text{ox}}^{(4)}$ on λ_{Edd} in the right panel of Fig. 2. The widespread presence of the warm corona covering the accretion disk in Mkn 590 [72] can significantly modulate the overall shape of the SED, and hence have a strong impact on the newly defined $\alpha_{\text{ox}}^{(0.5)}$ parameter. In contrast, $\alpha_{\text{ox}}^{(4)}$ is not impacted by the soft excess, as it explores hot coronal emission only. The absence of a clear ‘V’-shaped trend and the lack of detected break points in the $\alpha_{\text{ox}}^{(0.5)} - \lambda_{\text{Edd}}$ relation clearly highlight its diverging behavior compared to standard α_{ox} . It suggests a tight radiative and possibly structural coupling between the warm corona and the UV-emitting disk. On the other hand, $\alpha_{\text{ox}}^{(4)}$ exhibits the expected ‘V’-shaped trend similar to that displayed in the left panel. This indicates that the 2 and 4 keV fluxes are dominated by the hot coronal power-law component and are not significantly contaminated by the SXE emission. Overall, the three observed trends

⁵https://github.com/cjekel/piecewise_linear_fit.py

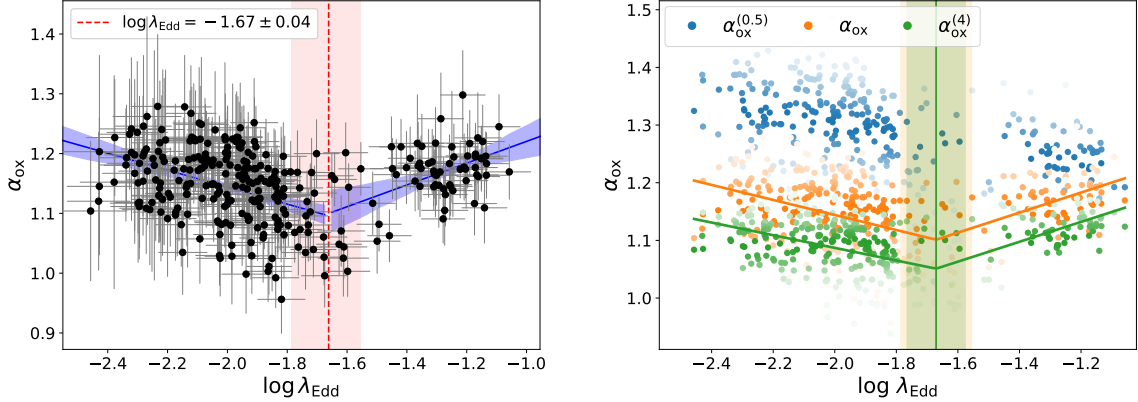


Fig. 2 *Left:* the variation of α_{ox} with λ_{Edd} from *Swift* monitoring of Mkn 590 from Dec. 10, 2013 to Sept. 28, 2025. The scatter of data exhibits a ‘V’-shaped trend, with a break point indicated by the vertical red dashed line. The associated 95% confidence interval is shown as a red shaded band. Linear fits on either side of the break point are indicated by solid blue lines, while their 95% confidence region are shown in purple shading. *Right panels:* the same variation, but for $\alpha_{\text{ox}}^{(0.5)}$ shown in blue, α_{ox} in orange, and $\alpha_{\text{ox}}^{(4)}$ in green points. Points are color coded by point density to highlight regions of higher concentration and improve visualization of the underlying trend. In the case of $\alpha_{\text{ox}}^{(4)}$, a turnover was detected at $\log \lambda_{\text{Edd}} = -1.67 \pm 0.04$, a value identical to that for the α_{ox} relation and is shown by vertical lines together with their confidence intervals as shaded regions. In the case of $\alpha_{\text{ox}}^{(0.5)}$, no such break point was found.

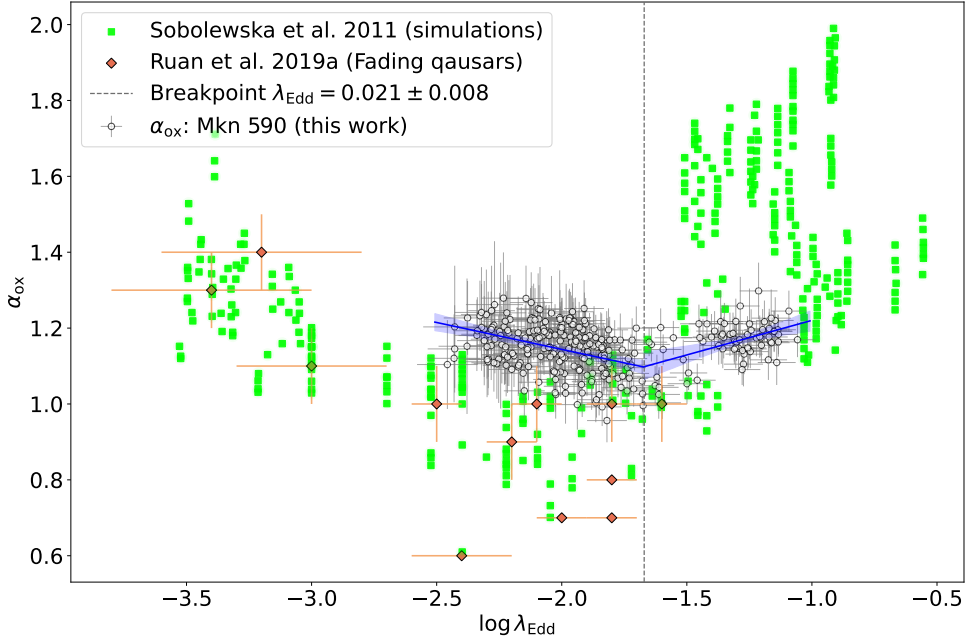


Fig. 3 A comparison of the observed $\alpha_{\text{ox}}-\lambda_{\text{Edd}}$ relation (with L_{bol} computed by the SED integration method) for Mkn 590 given by open circles, with observations of several fading quasars marked by red diamonds [39], and with simulated predictions for AGN marked by green squares [23]. The vertical dashed line represents the break point of the observed relation (see Fig. 2), while blue lines show linear fits to the data, with shaded regions indicating 1σ confidence intervals.

support the presence of distinct emission components within the accretion flow around SMBHs, with the hot and warm corona coupling to the disk in distinct ways.

In order to test the robustness of the observed α_{ox} evolution against the choice of tracers of accretion power, we used the ratio $\lambda L_{2500}/L_{\text{Edd}}$, which primarily traces thermal emission from an accretion disk in UV, and the ratio $L_{\text{X}}/L_{\text{Edd}}$, where L_{X} is the integrated 2–10 keV luminosity representing the power from the hot corona. The dependence of α_{ox} on the UV and X-ray tracers is shown in the left and right panels of Fig. 4, respectively. Again, ‘V’-shaped relations persist for both tracers. The best fit linear models for the left and right arms of the $\alpha_{\text{ox}} - \log(\lambda L_{2500}/L_{\text{Edd}})$ relation are $\alpha_{\text{ox}} = (-0.05 \pm 0.03) \log(\lambda L_{2500}/L_{\text{Edd}}) + (0.98 \pm 0.07)$ and $\alpha_{\text{ox}} = (0.09 \pm 0.02) \log(\lambda L_{2500}/L_{\text{Edd}}) + (1.34 \pm 0.04)$ respectively. Similarly, for the $\alpha_{\text{ox}} - \log(L_{\text{X}}/L_{\text{Edd}})$ relation, $\alpha_{\text{ox}} = (-0.15 \pm 0.02) \log(L_{\text{X}}/L_{\text{Edd}}) +$

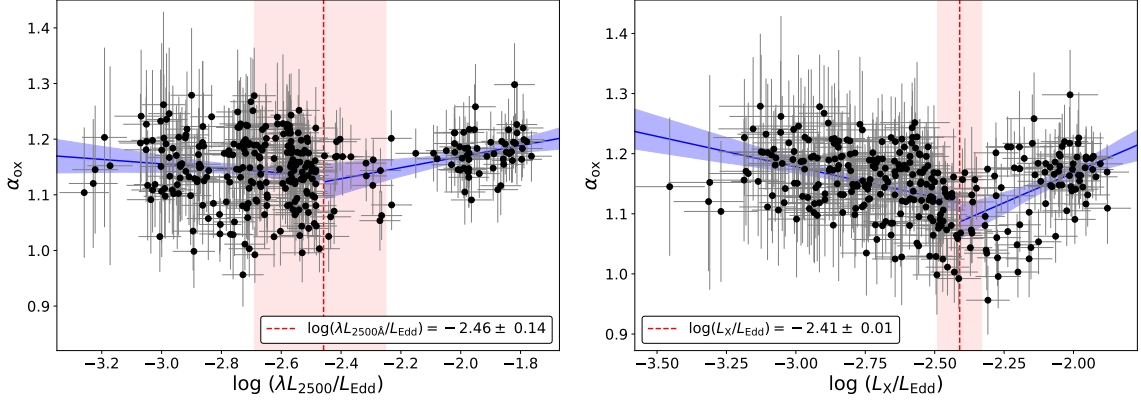


Fig. 4 The dependence of α_{ox} on the UV and hard X-ray accretion power tracers $\lambda L_{2500}/L_{\text{Edd}}$ and L_X/L_{Edd} . The meaning of colors is the same as in the left panel of Fig. 2.

(0.73 ± 0.05) and $\alpha_{\text{ox}} = (0.25 \pm 0.04) \log(L_X/L_{\text{Edd}}) + (1.67 \pm 0.08)$ respectively. It is worth noting that the linear relations based on the UV accretion power tracer are more shallow than the reference relation of $\alpha_{\text{ox}} - \lambda_{\text{Edd}}$ in Fig. 2, while the relations based on X-ray accretion have comparable slopes to that of the reference one. Remarkably, both the relations in Fig. 4 exhibit comparable values for the turnover, with statistically significant break points at $\log(\lambda L_{2500}/L_{\text{Edd}}) = -2.46 \pm 0.14$ and $\log(L_X/L_{\text{Edd}}) = -2.41 \pm 0.01$, respectively, as indicated by the vertical dashed lines and shaded regions. The close agreement between these independently derived break points reinforces the physical nature of the transition in CLAGNs and further discussed in Sec. 7.

5 Hardness–Intensity Diagram

As an attempt to identify evolutionary tracks in an AGN accretion flow, we examine the HID of Mkn 590 and assess whether the source exhibits evidence of the state transition analogous to the canonical spectral state changes observed in XRBs. The top panel of Fig. 5 presents the light curve of λ_{Edd} in Mkn 590 from year 2014 to 2025, derived from the *Swift* data. The light curve is segmented into broad phases (A–D) and finer sub-epochs (e.g., B1–B8), each color coded for consistency across subsequent analyses. The sharp increase in λ_{Edd} starting early 2024 is highlighted in black and marks a distinct transition in an accretion pattern.

A more detailed examination of the interplay between the emission components is presented in the middle row of Fig. 5, which shows the evolution of λ_{Edd} as a function of HR (left and center panels), and α_{ox} (right panel). The data points are color coded according to the temporal segments defined in the top panel. The red dashed line indicates the break point in the $\alpha_{\text{ox}}-\lambda_{\text{Edd}}$ relation determined in Sec. 4. In the leftmost $\lambda_{\text{Edd}}-HR$ plot, the source traces a broadly concave trajectory, reminiscent of the characteristic color–color diagrams observed in XRBs [85, and references therein], where accreting systems generally evolve from harder to softer states with increasing luminosity. For better visualization of temporal evolution, the data are binned by segments, with arrows indicating the direction of progression through time, as shown in the middle and right panels. The value of HR determines the dominance of hard X-rays over the soft X-rays and in this case, as evidenced from the middle panel, the source was relatively more variable in hard X-rays between 2014–2023. Starting from the faintest state (A), it traced out an irregular loop (B1–B8) while remaining restricted to relatively low values of HR , and with variability temporarily following a harder-when-brighter trend. For the same epochs, α_{ox} also traced out an irregular loop (B1–B8) evolving towards lower values of α_{ox} , indicating a relative dominance of hard X-rays over the thermal UV emission. Historically, as well as in the top panel, this period is marked by the characteristic flaring activity seen in optical/UV and X-rays, gradually approaching the pre-flare dip at B8. A major contrast appears in these plots for the point of transition between regions B8 and C, where the value of HR does not vary much while α_{ox} drops to minimal values, corresponding to the ‘V’-shaped break point previously presented. From C onward, the source rapidly evolves along a distinct branch, characterized by the high/soft values of both HR and α_{ox} , and thus switching to a softer-when-brighter behavior. This switch signals a change in emission mechanisms before and after C, likely caused by change in disk-corona structure, further discussed in Sec. 7.2.

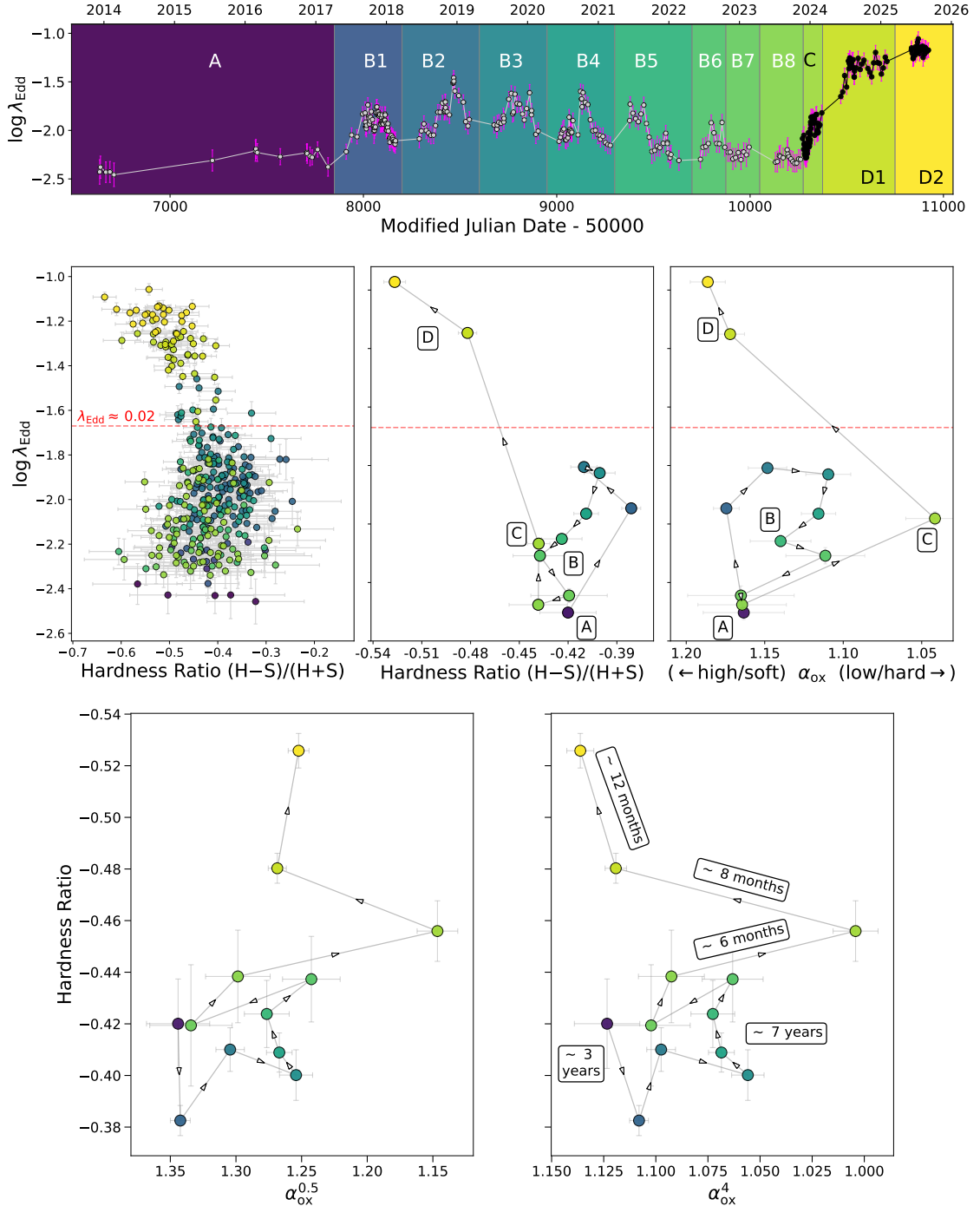


Fig. 5 *Top:* The light curve of λ_{Edd} , segmented into time slots named from A to D2, and color coded for reference to the following sub-panels below. *Middle:* From left to right: λ_{Edd} versus HR for all *Swift* data, the same but binned across color coded time slots, and λ_{Edd} versus α_{ox} relation binned in the same way, respectively. *Bottom:* Binned HR vs $\alpha_{\text{ox}}^{(0.5)}$ (right) and $\alpha_{\text{ox}}^{(4)}$ (left) relations showing similarly the coupled behavior of UV-thermal disk with warm corona, and warm with hot corona. The approximate timescales correspond to epochs A → B1, B1 → B8, B8 → C, C → D1 and D1 → D2, respectively.

In the bottom row, we further explored the coupling between thermal and non-thermal emission components by plotting HR against the two new X-ray loudness parameters $\alpha_{\text{ox}}^{(0.5)}$ and $\alpha_{\text{ox}}^{(4)}$. The meaning of those two plots is that towards the lower left regions of the plots, we expect relatively stronger harder X-ray emission together with relatively stronger UV disc emission than the coronae. Movement towards the top of the plot means the warm corona gets relatively stronger or that hard X power law gets steeper, and movement towards the right means that UV disc emission gets relatively weaker. The rightmost panel includes annotations of approximate timescales derived from the light

curve in the top panel. The source passes through multiple accretion regimes over timescales ranging from months to years, driven by a complex interplay between the thermal disk, warm corona, and hot corona. We further discuss these in the context of the source evolution and its state transition in Sec. 7, assuming that the term “soft” is reserved for disk dominance and the term “hard” for hot corona dominance, since it is based on the meaning of the α_{ox} parameter.

6 The Location of Mkn 590 on the Fundamental Plane

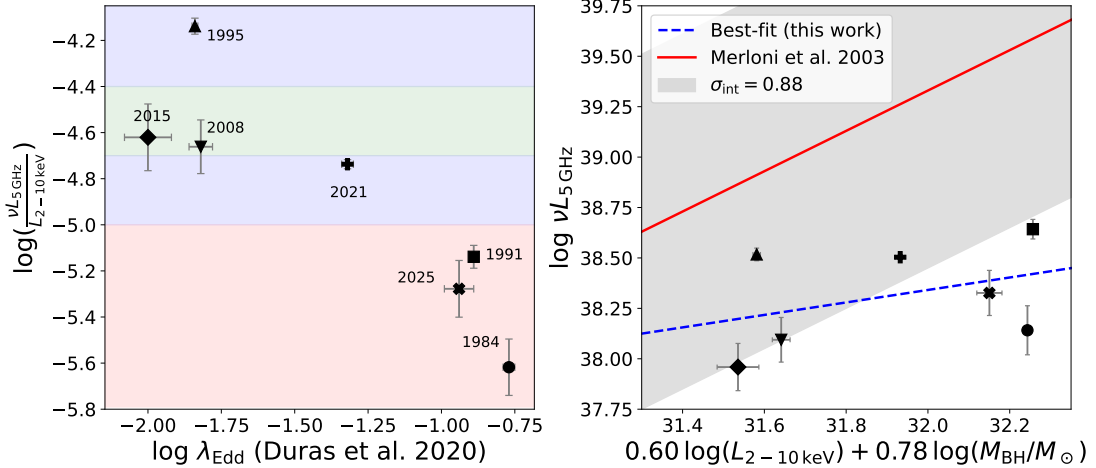


Fig. 6 *Left:* The variation of the radio-to-X-ray luminosity ratio with λ_{Edd} , based on the data presented in Tab. 1. A clear evolutionary trend is shown across epochs. Shaded colors reflect the same activity states as marked in Fig. 1: red, blue, and green, denote bright, intermediate and faint states, respectively. *Right:* Comparison of Mkn 590 against the empirical relation of FP [49], represented by a solid red line with its intrinsic scatter as a grey shaded region. The blue dashed line represents a linear fit to the data of Mkn 590. Identical marker symbols are used in both panels to represent the same observational epochs.

The well established Fundamental Plane (FP) of black hole activity supports the idea that XRBs and AGN are scale-invariant systems, linking the M_{BH} , X-ray and radio luminosity across several orders of magnitude [49]. We investigate the evolution of the radio-to-X-ray luminosity ratio against the λ_{Edd} , place the source on the FP, based on the luminosities listed in Tab. 1 and discuss the trends further in Sec. 7.3. Due to the lack of full SED coverage for most epochs, we adopted the hard X-ray bolometric correction method [86] to estimate L_{bol} (further details in Appendix B.1), ensuring uniformity across the dataset. The left panel of Fig. 6 shows a variation of the radio emission strength relative to the X-rays across different activity states, the same as defined for Fig. 1. A clear trend emerges, where the radio emission is strongest during faint and intermediate states (e.g., 1995, 2008, and 2015), while it is suppressed during the bright states (1984, 1991, and 2025). This behavior is broadly consistent with the AGN/XRB analogy, wherein compact, steady jets are associated with the low/hard states and become quenched during the high/soft states.

The location of Mkn 590 at the FP is shown in the Fig. 6 (right panel) where it maintains a positive correlation extending over the current bright state. The best-fit linear relation (indicated by the blue dashed line) exhibits a slope $\sim 70\%$ shallower compared to the canonical empirical FP relation derived by [49]. This could be an artifact of our work due to having a wider flux variability in X-rays as compared to radio. However, a similar deviation was reported for another proto-typical CLAGN, Mrk 1018 [46], suggesting that CLAGN may systematically diverge from the standard FP relation derived for low luminosity AGN and XRBs in the low/hard state.

7 Discussions and conclusion

For decades, the effort to unify accretion physics across the black hole mass spectrum from stellar mass black holes in XRBs to SMBH in AGNs has represented one of the central challenges in high energy astrophysics. However, the discovery of extreme AGN variability, particularly in Changing-Look AGN, has revolutionized this pursuit. These rare sources now offer a unique window into the dynamic evolution of accretion flows onto SMBHs, on observationally accessible timescales. In this

study, we investigate a CL event in the AGN Mkn 590, searching for evidence of accretion state transitions analogous to those observed in XRBs. Utilizing comprehensive multi-epoch monitoring from the *Neil Gehrels Swift Observatory*, along with nearly fifty years of archival multi-band data, we conduct a series of diagnostic analyses to evaluate the spectral and temporal evolution of Mkn 590 in the context of its spectral state transition. We first investigate the $\alpha_{\text{ox}} - \lambda_{\text{Edd}}$ relation, identifying a characteristic ‘V’-shaped profile indicative of structural changes in the accretion flow. We also use alternate versions of α_{ox} to specifically look into the connection between warm/hot coronae with the UV-emitting thermal disk. Next, we track the source’s path in the hardness–intensity diagram, comparing its trajectory to XRB-like state transitions. Finally, we place Mkn 590 on the Fundamental Plane of black hole activity to explore its accretion–ejection behavior in the broader context of black hole unification.

7.1 Evidence for an XRB-like state transition

As discussed in Sec. 4 and illustrated in Fig. 2, Mkn 590 shows a clear ‘V’-shaped trend with a statistically robust break point at $\lambda_{\text{Edd}} = 0.021 \pm 0.008$ that further aligns closely with the break points identified in other accreting compact objects (Fig. 3). This value has been interpreted as marking a structural transition in the inner accretion flow: from a geometrically-thick, radiatively inefficient, optically-thin advection-dominated accretion flow (ADAF; [9, 87]) below $\lambda_{\text{Edd}} \lesssim 0.01$, to a standard thin disk at higher accretion rates. As the source increases in accretion rate, the disk approaches the innermost stable circular orbit, and the UV emission strengthens rapidly, α_{ox} reverses its trend, forming a ‘V’-shaped profile. This characteristic shape thus traces the switch between a radiatively inefficient and a efficient accretion regimes, serving as a robust observational marker of spectral state transitions analogous to those seen in XRBs. Since Mkn 590 was not observed by *Swift* at lower accretion rates prior to 2013, the extreme low-luminosity end of this diagnostic plot remains unconstrained. While direct confirmation of an ADAF state is lacking, the observed softening of α_{ox} at low Eddington ratios provides indirect support for such a scenario. The right side of the relation in Mkn 590 coincides with a strongly emitting warm corona, reminiscent of the very high/soft states in XRBs where hybrid Comptonization models are required, as seen in XRBs such as GRO J1655-40 and GRS 1915+105 [88, 89]. Warm coronal components have also been detected in the hard state of Cyg X-1 [90], suggesting their presence across multiple accretion regimes. These parallels further support structural similarities between AGN and XRB accretion flows.

In contrast to the standard α_{ox} and $\alpha_{\text{ox}}^{(4)}$ trends shown in Fig. 2, the $\alpha_{\text{ox}}^{(0.5)} - \lambda_{\text{Edd}}$ relation exhibits a divergent behavior, showing no clear break point. The shared variability between the thermal disk and the warm corona suggests a tighter radiative coupling between these components, causing the observed continuous declining trend for the $\alpha_{\text{ox}}^{(0.5)} - \lambda_{\text{Edd}}$ relation. This notion agrees with the previously proposed geometries for the inner accretion flow, where the warm corona is situated on top of a passive accretion disk [5, 91]. Additionally, magnetic energy dissipation in accretion disks has been shown to naturally produce such optically-thick warm layers in both AGNs and XRBs [92]. This configuration enables efficient Compton up-scattering of UV seed photons, enhancing the soft X-ray excess and contributing significantly to the ionizing radiation field. Meanwhile, a warm corona was already present at $\lambda_{\text{Edd}} \sim 0.01$, though the SXE flux remained weak [72]. Only in the most recent epochs – since early 2024 – did the SXE flux strengthen significantly, possibly indicating that the warm corona became dissipative as the source transitioned into a higher accretion state [38].

Using independent tracers of accretion power, $\log(\lambda L_{2500}/L_{\text{Edd}})$ and $\log(L_{\text{X}}/L_{\text{Edd}})$, we find a consistent break point at $\lambda_{\text{Edd}} \sim 0.004$. Comparable break point values using $\log(\lambda L_{2500}/L_{\text{Edd}})$ as a tracer have been reported in other well-studied CLAGNs such as NGC 2617 and ZTF18aaajupnt [42]. In a recent study of SXE evolution on a sample of CLAGNs, a turnover at $\log \lambda_{\text{Edd}} = -2.47 \pm 0.09$ in the hot corona photon index (Γ) vs λ_{Edd} plane was reported [93], consistent with earlier findings in both high- and low-luminosity AGNs [94]. Interpreted within this framework, the emission mechanisms in both UV and X-rays appear to undergo changes beyond this critical monochromatic Eddington ratio. Future broadband SED modeling of the low accretion regime will be crucial for disentangling the underlying emission processes. However, it is worth noting that XRB spectral models predict a substantially lower break point in α_{ox} versus $\log(\lambda L_{2500}/L_{\text{Edd}})$ relation, displaying a break at ~ -3.5 [Fig. 3 in 42], suggesting that CLAGN and CL-quasars may follow distinct disk-corona coupling patterns depending on their luminosity class and spectral type, and that direct comparisons require careful spectral modeling.

7.2 Distinct accretion regimes

The rapid rise in Eddington fraction in 2024 (Fig. 5, top) occurring within ~ 8 months is reminiscent of the outbursts seen in XRBs, which are followed by a transition from quiescence to the bright state. The HID and X-ray loudness parameter of Mkn 590 reveal a clear sequence of distinct spectral states (Sec. 5). Below we interpret the four temporal segments, A→D, identified in Fig. 5 in chronological order. They are defined by characteristic spectral signatures, emission component dominance, and physical timescales.

A – Dec. 2013 to Mar. 2017 – Faint soft state. The source is in a low accretion phase, with $\lambda_{\text{Edd}} \sim 0.003 – 0.004$, most probably in the form of an ADAF-like inner hot flow with the disk truncated at larger radii [9, 87]. In such a scenario, the disk emission may be weak, but additional UV flux may originate from synchrotron emission of a weak jet or free-free emission from the outer part of the ADAF, leading to further softening of α_{ox} [56]. Moreover, there is evidence for a minor hardening in the spectrum of the hot corona with an increase of accretion rate: [62] reported a value of $\Gamma = 1.67 \pm 0.01$ in 2011 using *Suzaku* data, while Γ was reported to be 1.6 ± 0.1 in 2014 by [58] using *Chandra*. Such behavior reflects the $\Gamma – \lambda_{\text{Edd}}$ trend observed before the break point at $\log \lambda_{\text{Edd}} \sim -2.46$ for sample studies of AGNs and CLAGNs [82, 94].

B – Mar. 2017 to Oct. 2023 – Flaring intermediate state. The source displayed fluctuations in λ_{Edd} accompanied by multi-wavelength variability on the timescales of months to a year, consistent with the thermal timescales operating in the inner disk with viscosity parameter of $\sim 0.033 – 0.1$ [61]. The irregular loop generally follows a harder-when-brighter behavior, but additionally displays an irregular loop, which is similar to hysteresis seen at the lower luminosity branch in HIDs of XRBs.

C – Oct. 2023 to Mar. 2024 – Intermediate hard state. The UV flux dropped sharply in comparison to X-rays, while *HR* softened slightly. This suggests a temporary suppression or restructuring of the inner thermal disk. As shown in Fig. 1, the subsequent stages of evolution saw a rise in SXE flux by two orders of magnitude which points to changes in the warm corona geometry: likely enhancing its interception of UV seed photons, similar to what was observed in the CLAGN Mrk 1018 [41] and consistent with sample studies of un-obsured Seyferts [47]. Since the warm corona was already present during the flaring state (B), it could also suggest a switch from a low dissipative to strongly dissipative nature during this state. The change from B8→D1 through C, covering the transition via the critical value of $\lambda_{\text{Edd}} = 0.021$ determined in this work, takes 14 months. A comparable timescale has been reported for another CLAGN, 1ES 1927+654 [37, 95], supporting one possible interpretation that magnetically-supported or magnetically-elevated accretion disks can enable faster transitions than expected from classical viscous timescales.

D – July 2024 to Aug. 2025 – Bright soft state. This represents the current state of the source, marked by a sharp rise in λ_{Edd} , where the overall emission is dominated by soft X-rays and a relative dominance of UV emission over hard X-rays (lower panels of Fig. 5). This state resembles the high/soft phase in XRBs, and indicates strong thermal disk emission driving re-ionization of the BLR and the recent re-strengthening of the broad Balmer lines [38].

Overall, Mkn 590 is a recurring CLAGN, having showcased three CL events in ~ 50 years (Fig. 1). The gradual dimming starting in the mid-1990s lasted for ≈ 20 years until 2015 (A in Fig. 5). As shown in Fig. 5 (bottom), during the last decade, the timescales ranged between months to years, and were associated with different accretion phases discussed above. The total time span between the end stages of fading (A) and then complete reawakening (D2) is ~ 10 years. The timescales constrained from sample studies of CLAGNs indicate a ‘turn-off’ to ‘turn-on’ time difference of 5–20 years [33, 96, 97], with the ‘turn-off’ phase lasting longer than ‘turn-on’ phase [34], which is consistent with our results. While the exact ‘triggering’ mechanism remains unclear, the CL-transition is followed by formation of a dissipative warm corona and its timescales are consistent with thermally driven instabilities in the disk as discussed above.

7.3 Long term radio/X-ray variability

Here, we interpret the long-term X-ray and radio variability of Mkn 590 over the past five decades (Fig. 1). As noted by [56], assessing intrinsic variability in the GHz radio band is complicated by the use of instruments with differing beam sizes. To minimize these uncertainties, we selected seven epochs with comparable beam sizes and quasi-simultaneous X-ray and radio observations (Tab. 1), to assess the long-term radio-X-ray connection.

The radio-to-X-ray luminosity ratio exhibits a clear decline with increasing accretion rate (Fig. 6, left), consistent with a transition toward the high/soft accretion state. During the faint phase,

Mkn 590 displayed $\log(\nu L_{5,\text{GHz}}/L_{2-10,\text{keV}}) \lesssim -4.5$, a value commonly associated with compact, low-power jets in low-luminosity AGNs [98]. This aligns with VLBA detections of a parsec-scale jet in Mkn 590 around 2015 [65], suggesting that the observed radio emission at low Eddington ratios likely includes a jet contribution. As the accretion rate increases, the radio output becomes increasingly suppressed, consistent with the quenching of jet activity and the dominance of a radiatively efficient accretion flows, as observed in the high/soft states of XRBs.

Notably, as shown in Fig. 1, a delayed radio re-brightening had occurred in the mid-1990s (detected with comparable beam sizes; see Tab. 2), following the X-ray luminosity increase that began in the late 1980s. If this historical evolution represents a state transition to the bright (high/soft) state analogous to the recent epochs, then the subsequent radio flare may be interpreted as a transient jet or outflow event. Such an event could be triggered by the ejection or disruption of the inner Comptonizing region, causing a shocked outflow, and resulting in larger variability in the GHz band, arising from coronal activity $\log(\nu L_{5\text{GHz}}/L_{2-10\text{keV}}) \sim -5$, during the bright state [56, 99]. This interpretation is further supported by observations of XRBs, in which transitions from hard to soft spectral states are frequently associated with the suppression or disappearance of the compact Comptonizing corona and the subsequent launch of discrete, optically thin, relativistic ejecta detectable in the radio band. This behavior is especially well-documented in the case of GRS 1915+105 [43, 100]. As shown in the *Swift* X-ray/UV light curves, a short period, pre-flare dip was detected in Mkn 590 (also see Fig. 5, top panel, B8). In GRS 1915+105, similar X-ray dips have been temporally linked to the onset of infrared and radio flares, and interpreted as signatures of matter being expelled from the inner disk [101, 102]. Hence, if Mkn 590 is currently undergoing a similar accretion cycle as suggested by the moderate rise in radio flux density detected in early 2025 [67], a comparable delayed radio flare may be imminent, similar to observations of the CLAGN 1ES 1927+654 [103]. This reinforces the need for sustained, high-cadence monitoring of the source in both radio and X-ray bands over the coming years, which could offer a rare opportunity to directly capture jet reactivation linked to state evolution in Seyfert galaxies.

Bright Seyferts almost invariably exhibit significant coronal X-ray emission [104], in contrast to XRBs in which the emission can become overwhelmingly disk-dominated in the high/soft state. As argued by [105], jet activity in CLAGN is strongly coupled to the X-ray-emitting corona which explains the persistence of detectable weak radio emission even in high-luminosity states. This can explain the shallow slope observed in CLAGNs and points towards a fundamental structural distinction between the accretion and ejection mechanisms in the two classes of objects.

7.4 On systematic biases in bolometric corrections for CLAGN

We show in Appendix B that care must be exercised when determining the bolometric luminosity of AGN with dramatic variability amplitudes, such as CLAGN. Existing standard bolometric correction schemes, although carefully determined based on large samples of high-quality data, inherently assume the intrinsic SED is the same for all AGN and that the SED does not change during the mild source variability. In addition, the bolometric corrections are based on type 1 AGN with significant X-ray detections, which potentially selects X-ray brighter AGN, and the sample does not include many, if any, AGN with dramatic source variability as we see for Mkn 590.

Comparing with the bolometric luminosity measured by integrating over the *Swift*-observed SED, we find standard bolometric correction factors tend to overestimate the bolometric luminosity for Mkn 590 by factors of 2 to 3 (0.35 - 0.5 dex; Fig. 8). The offsets are significant at the 4.5-5 σ level. If used to represent the Eddington luminosity ratio in the $\alpha_{\text{ox}} - \lambda_{\text{Edd}}$ relation, the break point would be significantly overestimated. This emphasizes that for better constraints on the underlying physics of AGN, directly measured L_{bol} values are preferred when the relevant observations are available.

Declarations

Data availability. The *Swift* data are publicly available via the *Swift* archive at the UK Solar System Data Centre (https://www.swift.ac.uk/swift_portal). The GMRT data is available at GMRT Online Archive (<https://naps.ncra.tifr.res.in/goa/data/search>) under the proposal ID- ddtC413. The NOT/ALFOSC data is downloadable from [doi:10.5281/zenodo.1868499](https://doi.org/10.5281/zenodo.1868499). The long term archival X-ray data presented in this work was retrieved from the XMM-Newton Upper limit server. The long term archival optical/UV/radio measurements presented were adopted from published works as detailed in the main text.

Acknowledgments. BP has been fully and AR has been partially supported by Polish National Science Center (NCN) grant No. 2021/41/B/ST9/04110. AM acknowledges support from NCN grant 2018/31/G/ST9/03224. MV, DL and GW acknowledge financial support by the Independent Research Fund Denmark via grants DFF-8021-0013 and DFF-3103-00146. Also, this work has benefited from Swift observing programs supported by the Instrument Centre for Danish Astronomy. DL acknowledges support from NASA grant 22-SWIFT22-0029 for this work. AB acknowledges the support of the EU-ARC.CZ Large Research Infrastructure grant project LM2023059 of the Ministry of Education, Youth and Sports of the Czech Republic. MS acknowledges Czech Science Foundation (GAČR) grant no. 26-23342I. KXL acknowledges financial support from the National Natural Science Foundation of China (12573020), and the Young Talent Project of Yunnan Province. BP acknowledges Dr. Sandra Raimundo for insightful discussions during the early stages of this work, and Dr. Swayantra Panda for kindly providing access to the DESI spectrum.

Author contributions statement. This work is based on more than a decade of public *Swift* monitoring observations initiated by numerous members of the community, in particular D.L. and M.V. The core analysis was enabled by data secured by M.V., D.L. and G.W. B.P. led the X-ray/UV data reduction, performed the primary analysis, and wrote the manuscript. The investigation of the long-term variability in α_{ox} was independently initiated by B.P. and D.L. B.P. A.R. and A.G.M. advanced the study to cover accretion state transitions and comparisons with X-ray binaries. Everyone contributed through scientific discussions, critical feedback, and manuscript input that shaped the interpretation and presentation of the results. The hardness-intensity diagram analysis benefited in particular from contributions by A.R. and A.G.M., while M.V. contributed substantially to the bolometric correction methodology presented in Sec. 7.4 and Appendix B. M.V. and D.L. provided the Mkn 590 host galaxy spectrum used in the analysis. J.J.R. provided the archival data essential for Fig. 3. G.W. and A.B. provided feedback on the radio analysis. T.S. provided input on the X-ray/UV analysis. A.B. led the reduction and analysis of the GMRT and ASKAP/VAST radio datasets. M.S. contributed to the modeling of the NOT/ALFOSC and DESI spectra. K.-X.L. contributed to an early discussion that was motivated by long-term optical monitoring of the source.

Competing interests. The authors declare no competing interests.

References

- [1] Shakura, N. I. & Sunyaev, R. A. Black holes in binary systems. Observational appearance. *Astron. Astrophys.* **24**, 337–355 (1973).
- [2] Haardt, F. & Maraschi, L. A Two-Phase Model for the X-Ray Emission from Seyfert Galaxies. *Astrophys. J. Lett.* **380**, L51 (1991).
- [3] Laor, A., Fiore, F., Elvis, M., Wilkes, B. J. & McDowell, J. C. The Soft X-Ray Properties of a Complete Sample of Optically Selected Quasars. II. Final Results. *Astrophys. J.* **477**, 93–113 (1997).
- [4] Różańska, A., Malzac, J., Belmont, R., Czerny, B. & Petrucci, P.-O. Warm and optically thick dissipative coronae above accretion disks. *Astron. Astrophys.* **580**, A77 (2015).
- [5] Petrucci, P.-O. *et al.* Testing warm Comptonization models for the origin of the soft X-ray excess in AGNs. *Astron. Astrophys.* **611**, A59 (2018).
- [6] Zdziarski, A. A. *et al.* What Is the Black Hole Spin in Cyg X-1? *Astrophys. J. Lett.* **967**, L9 (2024).
- [7] Abbott, R. *et al.* Population of Merging Compact Binaries Inferred Using Gravitational Waves through GWTC-3. *Physical Review X* **13**, 011048 (2023).
- [8] Różańska, A. & Czerny, B. Vertical structure of the accreting two-temperature corona and the transition to an ADAF. *Astron. Astrophys.* **360**, 1170–1186 (2000).

[9] Esin, A. A., McClintock, J. E. & Narayan, R. Advection-Dominated Accretion and the Spectral States of Black Hole X-Ray Binaries: Application to Nova Muscae 1991. *Astrophys. J.* **489**, 865–889 (1997).

[10] Poutanen, J., Krolik, J. H. & Ryde, F. The nature of spectral transitions in accreting black holes: the case of CYG X-1. *Mon. Not. R. Astron. Soc.* **292**, L21–L25 (1997).

[11] Remillard, R. A. & McClintock, J. E. X-Ray Properties of Black-Hole Binaries. *Annu. Rev. Astron. Astrophys.* **44**, 49–92 (2006).

[12] Done, C., Gierliński, M. & Kubota, A. Modelling the behaviour of accretion flows in X-ray binaries. Everything you always wanted to know about accretion but were afraid to ask. *Astron. Astrophys. Rev.* **15**, 1–66 (2007).

[13] Homan, J. & Belloni, T. The Evolution of Black Hole States. *Astrophys. Space Sci.* **300**, 107–117 (2005).

[14] Körding, E., Falcke, H. & Corbel, S. Refining the fundamental plane of accreting black holes. *Astron. Astrophys.* **456**, 439–450 (2006).

[15] Fernández-Ontiveros, J. A. & Muñoz-Darias, T. X-ray binary accretion states in active galactic nuclei? Sensing the accretion disc of supermassive black holes with mid-infrared nebular lines. *Mon. Not. R. Astron. Soc.* **504**, 5726–5740 (2021).

[16] Svoboda, J., Guainazzi, M. & Merloni, A. AGN spectral states from simultaneous UV and X-ray observations by XMM-Newton. *Astron. Astrophys.* **603**, A127 (2017).

[17] Moravec, E. *et al.* Do radio active galactic nuclei reflect X-ray binary spectral states? *Astron. Astrophys.* **662**, A28 (2022).

[18] Zamorani, G. *et al.* X-ray studies of quasars with the Einstein Observatory II. *Astrophys. J.* **245**, 357–374 (1981).

[19] Tananbaum, H. *et al.* X-ray studies of quasars with the Einstein Observatory. *Astrophys. J. Lett.* **234**, L9–L13 (1979).

[20] Young, M., Elvis, M. & Risaliti, G. The X-ray Energy Dependence of the Relation Between Optical and X-ray Emission in Quasars. *Astrophys. J.* **708**, 1388–1397 (2010).

[21] Lusso, E. *et al.* The X-ray to optical-UV luminosity ratio of X-ray selected type 1 AGN in XMM-COSMOS. *Astron. Astrophys.* **512**, A34 (2010).

[22] Grupe, D., Komossa, S., Leighly, K. M. & Page, K. L. The Simultaneous Optical-to-X-Ray Spectral Energy Distribution of Soft X-Ray Selected Active Galactic Nuclei Observed by Swift. *Astrophys. J. Suppl. Ser.* **187**, 64–106 (2010).

[23] Sobolewska, M. A., Siemiginowska, A. & Gierliński, M. Simulated spectral states of active galactic nuclei and observational predictions. *Mon. Not. R. Astron. Soc.* **413**, 2259–2268 (2011).

[24] York, D. G. *et al.* The Sloan Digital Sky Survey: Technical Summary. *Astron. J.* **120**, 1579–1587 (2000).

[25] Strauss, M. A. *et al.* Spectroscopic Target Selection in the Sloan Digital Sky Survey: The Main Galaxy Sample. *Astron. J.* **124**, 1810–1824 (2002).

[26] Sánchez-Sáez, P. & Others. Alert Classification for the ALeRCE Broker System: The Light Curve Classifier. *Astron. J.* **161**, 141 (2021).

[27] Shanks, T. *et al.* The VLT Survey Telescope ATLAS. *Mon. Not. R. Astron. Soc.* **451**, 4238–4252 (2015).

[28] Homan, D. *et al.* Discovery of the luminous X-ray ignition eRASSt J234402.9–352640. I. Tidal disruption event or a rapid increase in accretion in an active galactic nucleus? *Astron. Astrophys.* **672**, A167 (2023).

[29] Ricci, C. & Trakhtenbrot, B. Changing-look active galactic nuclei. *Nature Astronomy* **7**, 1282–1294 (2023).

[30] Khachikian, E. Y. & Weedman, D. W. A New Cloud of Hydrogen Emission in a Bright Galactic Nucleus. *Astrophys. J. Lett.* **164**, L109 (1971).

[31] Osterbrock, D. E. Spectrophotometry of Seyfert 1 galaxies. *Astrophys. J.* **215**, 733–745 (1977).

[32] Osterbrock, D. E. Seyfert galaxies with weak broad H alpha emission lines. *Astrophys. J.* **249**, 462–470 (1981).

[33] Panda, S. & Śniegowska, M. Changing-look Active Galactic Nuclei. I. Tracking the Transition on the Main Sequence of Quasars. *Astrophys. J. Suppl. Ser.* **272**, 13 (2024).

[34] Guo, W.-J. *et al.* Changing-look active galactic nuclei from the dark energy spectroscopic instrument. ii. statistical properties from the first data release. *The Astrophysical Journal Supplement Series* **278**, 28 (2025). URL <https://doi.org/10.3847/1538-4365/adc124>.

[35] Antonucci, R. Unified models for active galactic nuclei and quasars. *Annu. Rev. Astron. Astrophys.* **31**, 473–521 (1993).

[36] Noda, H. & Done, C. Explaining changing-look AGN with state transition triggered by rapid mass accretion rate drop. *Mon. Not. R. Astron. Soc.* **480**, 3898–3906 (2018).

[37] Ricci, C. *et al.* The Destruction and Recreation of the X-Ray Corona in a Changing-look Active Galactic Nucleus. *Astrophys. J. Lett.* **898**, L1 (2020).

[38] Palit, B. *et al.* Markarian 590: the AGN awakens. *Mon. Not. R. Astron. Soc.* **540**, L14–L20 (2025).

[39] Ruan, J. J. *et al.* The Analogous Structure of Accretion Flows in Supermassive and Stellar Mass Black Holes: New Insights from Faded Changing-look Quasars. *Astrophys. J.* **883**, 76 (2019).

[40] Jana, A. *et al.* Broad-band X-ray observations of the 2018 outburst of the changing-look active galactic nucleus NGC 1566. *Mon. Not. R. Astron. Soc.* **507**, 687–703 (2021).

[41] Saha, T. *et al.* The Close AGN Reference Survey (CARS): Long-term spectral variability study of the changing-look AGN Mrk 1018. *Astron. Astrophys.* **699**, A205 (2025).

[42] Ruan, J. J. *et al.* Tracing the AGN/X-ray Binary Analogy with Light Curves of Individual Changing-Look AGN. *arXiv e-prints* arXiv:1909.04676 (2019).

[43] Fender, R. P., Belloni, T. M. & Gallo, E. Towards a unified model for black hole X-ray binary jets. *Mon. Not. R. Astron. Soc.* **355**, 1105–1118 (2004).

[44] de Bruyn, A. G. & Wilson, A. S. The radio properties of Seyfert galaxies. *Astron. Astrophys.* **64**, 433–444 (1978).

[45] Panessa, F. *et al.* The origin of radio emission from radio-quiet active galactic nuclei. *Nature Astronomy* **3**, 387–396 (2019).

[46] Lyu, B., Yan, Z., Yu, W. & Wu, Q. Long-term and multiwavelength evolution of a changing-look AGN Mrk 1018. *Mon. Not. R. Astron. Soc.* **506**, 4188–4198 (2021).

[47] Hagen, S. *et al.* Untangling the complex nature of AGN variability in Fairall 9. *Mon. Not. R. Astron. Soc.* **544**, 1012–1037 (2025).

[48] Elitzur, M. & Ho, L. C. On the Disappearance of the Broad-Line Region in Low-Luminosity Active Galactic Nuclei. *Astrophys. J. Lett.* **701**, L91–L94 (2009).

[49] Merloni, A., Heinz, S. & di Matteo, T. A Fundamental Plane of black hole activity. *Mon. Not. R. Astron. Soc.* **345**, 1057–1076 (2003).

[50] Antonucci, R. Unified models for active galactic nuclei and quasars. *Annu. Rev. Astron. Astrophys.* **31**, 473–521 (1993).

[51] Urry, C. M. & Padovani, P. Unified Schemes for Radio-Loud Active Galactic Nuclei. *Publ. Astron. Soc. Pac.* **107**, 803 (1995).

[52] Ferland, G. J., Korista, K. T. & Peterson, B. M. Optically Thin Thermal Emission as the Origin of the Big Bump in the Spectra of Active Galactic Nuclei. *Astrophys. J. Lett.* **363**, L21 (1990).

[53] Turner, T. J. & Pounds, K. A. The EXOSAT spectral survey of AGN. *Mon. Not. R. Astron. Soc.* **240**, 833–880 (1989).

[54] Voges, W. *et al.* The ROSAT all-sky survey bright source catalogue. *Astron. Astrophys.* **349**, 389–405 (1999).

[55] Denney, K. D. *et al.* The Typecasting of Active Galactic Nuclei: Mrk 590 no Longer Fits the Role. *Astrophys. J.* **796**, 134 (2014).

[56] Koay, J. Y., Vestergaard, M., Bignall, H. E., Reynolds, C. & Peterson, B. M. Parsec-scale radio morphology and variability of a changing-look AGN: the case of Mrk 590. *Mon. Not. R. Astron. Soc.* **460**, 304–316 (2016).

[57] Longinotti, A. L. *et al.* An X-ray look at the Seyfert 1 Galaxy Mrk 590: XMM-Newton and Chandra reveal complexity in circumnuclear gas. *Astron. Astrophys.* **470**, 73–81 (2007).

[58] Mathur, S. *et al.* The Changing-look Quasar Mrk 590 Is Awakening. *Astrophys. J.* **866**, 123 (2018).

[59] Raimundo, S. I. *et al.* Tracing the origin of the AGN fuelling reservoir in MCG-6-30-15. *Mon. Not. R. Astron. Soc.* **464**, 4227–4246 (2017).

[60] Mandal, A. K. *et al.* Changing look AGN Mrk 590: broad-line region and black hole mass from photometric reverberation mapping. *Mon. Not. R. Astron. Soc.* **508**, 5296–5309 (2021).

[61] Lawther, D. *et al.* Flares in the changing look AGN Mrk 590 - I. The UV response to X-ray outbursts suggests a more complex reprocessing geometry than a standard disc. *Mon. Not. R. Astron. Soc.* **519**, 3903–3922 (2023).

[62] Rivers, E., Markowitz, A., Duro, R. & Rothschild, R. A Suzaku Observation of Mkn 590 Reveals a Vanishing Soft Excess. *Astrophys. J.* **759**, 63 (2012).

[63] Ghosh, R. *et al.* The Origin of the Vanishing Soft X-Ray Excess in the Changing-look Active Galactic Nucleus Mrk 590. *Astrophys. J.* **937**, 31 (2022).

[64] Wilson, A. S. & Meurs, E. J. A. A 1415 MHz survey of Seyfert and related galaxies. III. *Astron. Astrophys. Suppl.* **50**, 217–231 (1982).

[65] Yang, J. *et al.* A parsec-scale faint jet in the nearby changing-look Seyfert galaxy Mrk 590. *Mon. Not. R. Astron. Soc.* **502**, L61–L65 (2021).

[66] Birmingham, S. *et al.* The birth of young radio jets in changing-look AGN: a population study. *arXiv e-prints* arXiv:2507.01355 (2025).

[67] Palit, B. *et al.* Optical and cm follow-ups of the Changing-Look event in Mkn 590. *arXiv e-prints* arXiv:2511.19660 (2025).

[68] Wright, E. L. A Cosmology Calculator for the World Wide Web. *Publ. Astron. Soc. Pac.* **118**, 1711–1715 (2006).

[69] Peterson, B. M. *et al.* Central Masses and Broad-Line Region Sizes of Active Galactic Nuclei. II. A Homogeneous Analysis of a Large Reverberation-Mapping Database. *Astrophys. J.* **613**, 682–699 (2004).

[70] Burrows, D. N. *et al.* The Swift X-Ray Telescope. *Space Sci. Rev.* **120**, 165–195 (2005).

[71] Roming, P. W. A. *et al.* The Swift Ultra-Violet/Optical Telescope. *Space Sci. Rev.* **120**, 95–142 (2005).

[72] Lawther, D., Vestergaard, M., Raimundo, S., Fan, X. & Koay, J. Y. Flares in the changing look AGN Mrk 590 – II. Deep X-ray observations reveal a Comptonizing inner accretion flow. *Mon. Not. R. Astron. Soc.* **539**, 501–541 (2025).

[73] Evans, P. A. *et al.* Methods and results of an automatic analysis of a complete sample of Swift-XRT observations of GRBs. *Mon. Not. R. Astron. Soc.* **397**, 1177–1201 (2009).

[74] Poole, T. S. *et al.* Photometric calibration of the Swift ultraviolet/optical telescope. *Mon. Not. R. Astron. Soc.* **383**, 627–645 (2008).

[75] Edelson, R. *et al.* The First Swift Intensive AGN Accretion Disk Reverberation Mapping Survey. *Astrophys. J.* **870**, 123 (2019).

[76] Schlegel, D. J., Finkbeiner, D. P. & Davis, M. Maps of Dust Infrared Emission for Use in Estimation of Reddening and Cosmic Microwave Background Radiation Foregrounds. *Astrophys. J.* **500**, 525–553 (1998).

[77] Cardelli, J. A., Clayton, G. C. & Mathis, J. S. The Relationship between Infrared, Optical, and Ultraviolet Extinction. *Astrophys. J.* **345**, 245 (1989).

[78] Condon, J. J. Radio emission from normal galaxies. *Annu. Rev. Astron. Astrophys.* **30**, 575–611 (1992).

[79] Sobolewska, M. A., Gierliński, M. & Siemiginowska, A. What can we learn about quasars from α_{OX} measurements in Galactic black hole binaries? *Mon. Not. R. Astron. Soc.* **394**, 1640–1648 (2009).

[80] Arnaud, K. A., Jacoby, G. H. & Barnes, J. (eds) *XSPEC: The First Ten Years*. (eds Jacoby, G. H. & Barnes, J.) *Astronomical Data Analysis Software and Systems V*, Vol. 101 of *Astronomical Society of the Pacific Conference Series*, 17 (1996).

[81] Pilgrim, C. piecewise-regression (aka segmented regression) in python. *Journal of Open Source Software* **6**, 3859 (2021). URL <https://doi.org/10.21105/joss.03859>.

[82] Jana, A. *et al.* Investigating changing-look active galactic nuclei with long-term optical and X-ray observations. *Astron. Astrophys.* **693**, A35 (2025).

[83] Gilbert, O. *et al.* Using Faded Changing-Look Quasars to Unveil the Spectral Energy Distribution Evolution of Low-Luminosity Active Galactic Nuclei. *arXiv e-prints* arXiv:2508.01933 (2025).

[84] Duffy, L., Eracleous, M., Ruan, J. J., Yang, Q. & Runnoe, J. C. Sleeping Giants Arise: Monitoring the Return of Three Changing-look Quasars to Their High States. *Astrophys. J.* **989**, 102 (2025).

[85] Kalemci, E., Kara, E. & Tomsick, J. A. in *Black Holes: Timing and Spectral Properties and Evolution* (eds Bambi, C. & Sangangelo, A.) *Handbook of X-ray and Gamma-ray Astrophysics* 9 (2022).

[86] Duras, F. *et al.* Universal bolometric corrections for active galactic nuclei over seven luminosity decades. *Astron. Astrophys.* **636**, A73 (2020).

[87] Narayan, R. & Yi, I. Advection-dominated Accretion: Underfed Black Holes and Neutron Stars. *Astrophys. J.* **452**, 710 (1995).

[88] Kubota, A., Makishima, K. & Ebisawa, K. Observational Evidence for Strong Disk Comptonization in GRO J1655-40. *Astrophys. J. Lett.* **560**, L147–L150 (2001).

[89] Zdziarski, A. A., Grove, J. E., Poutanen, J., Rao, A. R. & Vadawale, S. V. OSSE and RXTE Observations of GRS 1915+105: Evidence for Nonthermal Comptonization. *Astrophys. J. Lett.* **554**, L45–L48 (2001).

[90] Basak, R., Zdziarski, A. A., Parker, M. & Islam, N. Analysis of NuSTAR and Suzaku observations of Cyg X-1 in the hard state: evidence for a truncated disc geometry. *Mon. Not. R. Astron. Soc.* **472**, 4220–4232 (2017).

[91] Palit, B. *et al.* X-ray view of dissipative warm corona in active galactic nuclei. *Astron. Astrophys.* **690**, A308 (2024).

[92] Gronkiewicz, D. & Różańska, A. Warm and thick corona for a magnetically supported disk in galactic black hole binaries. *Astron. Astrophys.* **633**, A35 (2020).

[93] Jana, A. *et al.* Multi-wavelength properties of changing-state active galactic nuclei: I. the evolution of soft excess and X-ray continuum. *arXiv e-prints* arXiv:2601.07337 (2026).

[94] She, R., Ho, L. C., Feng, H. & Cui, C. Chandra Survey of Nearby Galaxies: Testing the Accretion Model for Low-luminosity AGNs. *Astrophys. J.* **859**, 152 (2018).

[95] Cao, X., You, B. & Wei, X. An accretion disc with magnetic outflows triggered by a sudden mass accretion event in changing-look active galactic nucleus 1ES 1927+654. *Mon. Not. R. Astron. Soc.* **526**, 2331–2340 (2023).

[96] Wang, S. *et al.* Dormancy and Reawakening over Years: Eight New Recurrent Changing-look AGNs. *Astrophys. J.* **981**, 129 (2025).

[97] Dong, Q. *et al.* Discovery of Repeating Transitions in 25 Changing-look Active Galactic Nuclei. *arXiv e-prints* arXiv:2510.18445 (2025).

[98] Terashima, Y. & Wilson, A. S. Chandra Snapshot Observations of Low-Luminosity Active Galactic Nuclei with a Compact Radio Source. *Astrophys. J.* **583**, 145–158 (2003).

[99] Gudel, M., Schmitt, J. H. M. M., Bookbinder, J. A. & Fleming, T. A. A Tight Correlation between Radio and X-Ray Luminosities of M Dwarfs. *Astrophys. J.* **415**, 236 (1993).

[100] Vadawale, S. V. *et al.* On the Origin of the Various Types of Radio Emission in GRS 1915+105. *Astrophys. J.* **597**, 1023–1035 (2003).

[101] Pooley, G. G. & Fender, R. P. The variable radio emission from GRS 1915+105. *Mon. Not. R. Astron. Soc.* **292**, 925–933 (1997).

[102] Mirabel, I. F. *et al.* Accretion instabilities and jet formation in GRS 1915+105. *Astron. Astrophys.* **330**, L9–L12 (1998).

[103] Meyer, E. T. *et al.* Late-time Radio Brightening and Emergence of a Radio Jet in the Changing-look AGN 1ES 1927+654. *Astrophys. J. Lett.* **979**, L2 (2025).

[104] Brandt, W. N. & Alexander, D. M. Cosmic X-ray surveys of distant active galaxies. The demographics, physics, and ecology of growing supermassive black holes. *Astron. Astrophys. Rev.* **23**, 1 (2015).

[105] Kang, J.-L. *et al.* Disk-jet coupling across the spectral transition in supermassive black holes. *Mon. Not. R. Astron. Soc.* (2025).

[106] van Groningen, E. & Wanders, I. An Algorithm for the Relative Scaling of Spectra. *Publ. Astron. Soc. Pac.* **104**, 700 (1992).

[107] Guo, H., Shen, Y. & Wang, S. PyQSOFit: Python code to fit the spectrum of quasars. Astrophysics Source Code Library, record ascl:1809.008 (2018). [1809.008](#).

[108] Mondal, S., Różańska, A., Bagińska, P., Markowitz, A. & De Marco, B. Spectral state transitions in Circinus ULX5. *Astron. Astrophys.* **651**, A54 (2021).

[109] Wilms, J., Allen, A. & McCray, R. On the Absorption of X-Rays in the Interstellar Medium. *Astrophys. J.* **542**, 914–924 (2000).

[110] MacLeod, C. L. *et al.* A systematic search for changing-look quasars in SDSS. *Mon. Not. R. Astron. Soc.* **457**, 389–404 (2016).

[111] Ross, N. P. *et al.* A new physical interpretation of optical and infrared variability in quasars. *Mon. Not. R. Astron. Soc.* **480**, 4468–4479 (2018).

[112] Rumbaugh, N. *et al.* Extreme Variability Quasars from the Sloan Digital Sky Survey and the Dark Energy Survey. *Astrophys. J.* **854**, 160 (2018).

[113] Wang, H. *et al.* Systematic Analysis of Changing-look AGN Variability Using ZTF Light Curves. *arXiv e-prints* arXiv:2511.10217 (2025).

[114] Muggeo, V. M. R. Estimating regression models with unknown break-points. *Statistics in Medicine* **22**, 3055–3071 (2003). URL <https://onlinelibrary.wiley.com/doi/abs/10.1002/sim.1545>.

[115] Muggeo, V. Segmented: An r package to fit regression models with broken-line relationships. *R News* **8**, 20–25 (2008).

[116] Wood, S. N. Minimizing model fitting objectives that contain spurious local minima by bootstrap restarting. *Biometrics* **57**, 240–244 (2004). URL <https://doi.org/10.1111/j.0006-341X.2001.00240.x>.

[117] Davies, R. B. Hypothesis testing when a nuisance parameter is present only under the alternatives. *Biometrika* **74**, 33–43 (1987). URL <http://www.jstor.org/stable/2336019>.

[118] Adcock, R. J. A problem in least squares. *The Analyst* **5**, 53–54 (1878). URL <http://www.jstor.org/stable/2635758>.

A Details on the historical data collection

Here, we detail on the multi-band data gathered across the entire history of the Mkn 590, and summarized in Tab. 2. Owing to the heterogeneous nature of the dataset, measurement uncertainties for the optical, UV, and X-ray fluxes are not uniformly available and are therefore not included. The long-term light curve shown in Fig. 1 is intended to illustrate the overall multi-wavelength variability trends only. Majority of the optical continuum fluxes are compiled from published studies (see last column), where full details of the observing campaigns are described in the cited papers and references therein. The NOT/ALFOSC spectrum was obtained through open calls for observation proposals (70-406; PI: B. Palit). The DESI and NOT/ALFOSC spectra is flux-normalized using the [O III] $\lambda 5007$ narrow emission line following the framework of [106], adopting as reference the line flux measured in the 2003 SDSS spectrum [38], and using the fitting software PYQSOFIT [107].

Both spectra are presented in [67] and will be analyzed in detail in a forthcoming study focused on broad-line region modeling.

The reported UV fluxes were obtained using broadband filters indicated in parentheses, and the continuum region corresponds to their respective effective wavelengths. Owing to the heterogeneous energy coverage of different X-ray instruments, we report fluxes integrated over their respective observing energy bands. For the purposes of the Fundamental Plane analysis (Sec. 2.2), the fluxes were converted to a uniform energy range using WebPIMMS tool. Between 2015–2025, we selected 2–4 *Swift*-XRT pointings per year to show the approximate trend in X-rays. The SXE measurements were only possible post-2000 and have been taken from [38, 63].

The radio observations vary in both beam size and continuum frequency, introducing non-uniformity in the historical light curve and the construction of the Fundamental Plane. To minimize potential biases, we restrict our sample to observations with arcsec-scale resolution and frequencies below 10 GHz.

Table 2: Mkn 590 continuum properties, used in this paper.

Observation Identifier	Year	Continuum Region	Continuum Flux ^d	Reference ^e
Optical Spectra ^a				
Lick IDS	1973	5100 Å	3.4	[55]
Perkins/OSU IDS	1983	5100 Å	11.0	[55]
RM campaign	1989	5100 Å	55.0	[55, 69]
RM campaign	1993	5100 Å	26.0	[55, 69]
RM campaign	1996	5100 Å	42.0	[55, 69]
SDSS	2003	5100 Å	1.30	[55]
MDM	2006	5100 Å	0.28	[55]
LBT MODS1	2013	5100 Å	< 0.014	[55]
LBT MODS1	2013	5100 Å	< 0.014	[55]
LBT MODS1	2013	5100 Å	< 0.014	[55]
KOSMOS	2013	5100 Å	< 0.10	[55]
MDM	2014	5100 Å	< 0.11	[55]
MUSE/VLT	2017	5100 Å	45.0	[59]
Subaru/HDS	2018	5100 Å	19.0	[108]
DESI	2022	5100 Å	4.35	[67]
LCO/FLOYD	2024	5100 Å	75.0	[38]
NOT/ ALFOSC	2025	5100 Å	118.0	[67]
UV Spectra ^b				
IUE	1982	1450 Å	88.5	[55]
IUE	1991	1450 Å	388.	[55]
XMM/OM (UVW2 filter)	2002	1928 Å	28.0	[63]
XMM/OM (UVW2 filter)	2004	1928 Å	26.0	[63]
Swift/UVOT (UVW2 filter)	2008	1928 Å	13.05	—
HST/COS	2013	1450 Å	3.7	[55]
HST/COS	2013	1450 Å	3.7	[55]
HST/COS	2013	1450 Å	3.7	[55]
Swift/UVOT (UVW2 filter)	2015	1928 Å	17.54	—
Swift/UVOT (UVW2 filter)	2017	1928 Å	33.68	—
Swift/UVOT (UVW2 filter)	2020	1928 Å	28.90	—
Swift/UVOT (UVW2 filter)	2022	1928 Å	14.45	—
Swift/UVOT (UVW2 filter)	2024	1928 Å	24.01	—
Swift/UVOT (UVW2 filter)	2025/03	1928 Å	175.20	—
Swift/UVOT (UVW2 filter)	2025/05	1928 Å	275.00	—
Swift/UVOT (UVW2 filter)	2025/09	1928 Å	300.00	—
X-ray Spectra ^c				
Einstein (HEAO-2)	1979	0.4–4 keV	13.9	†
Einstein (HEAO-2)	1979	0.4–4 keV	10	†
EXOSAT	1984	2–10 keV	27	[55]
RASS	1991	0.1–2.4 keV	46.3	[55]
ROSAT	1995	0.1–2.4 keV	3.47	†
ROSAT	1996	0.1–2.4 keV	11.0	†
XMM	2004	0.2–2 keV	3.31	[55]
XMM	2004	2–10 keV	6.95	[55]

Observation Identifier	Year	Continuum Region	Continuum Flux ^d	Reference ^e
Chandra	2004	0.5–10 keV	11.9	[55]
Swift/XRT	2008	2–10 keV	3.6	—
Suzaku/XIS+PIN	2011	2–10 keV	6.8	[55]
Chandra	2013	0.5–10 keV	1.3	[55]
Swift/XRT	2016/02	2–10 keV	4.9	—
Swift/XRT	2016/12	2–10 keV	5.0	—
Swift/XRT	2018	2–10 keV	14.8	—
Swift/XRT	2019	2–10 keV	21.8	—
Swift/XRT	2020/01	2–10 keV	20.9	—
Swift/XRT	2020/07	2–10 keV	10.8	—
Swift/XRT	2021/01	2–10 keV	10.9	—
Swift/XRT	2021/08	2–10 keV	18.8	—
Swift/XRT	2022/01	2–10 keV	3.8	—
Swift/XRT	2022/07	2–10 keV	9.9	—
Swift/XRT	2022/08	2–10 keV	7.7	—
Swift/XRT	2022/09	2–10 keV	9.9	—
Swift/XRT	2022/10	2–10 keV	6.1	—
Swift/XRT	2022/11	2–10 keV	6.2	—
Swift/XRT	2022/12	2–10 keV	5.2	—
Swift/XRT	2023/01	2–10 keV	5.0	—
Swift/XRT	2023/09	2–10 keV	5.5	—
Swift/XRT	2024/01	2–10 keV	21.5	—
Swift/XRT	2024/07	2–10 keV	20.5	—
Swift/XRT	2024/09	2–10 keV	28.2	—
Swift/XRT	2024/12	2–10 keV	36.6	—
Swift/XRT	2025/01	2–10 keV	27.1	—
Swift/XRT	2025/03	2–10 keV	19.20	—
Swift/XRT	2025/05	2–10 keV	44.0	—
Swift/XRT	2025/09	2–10 keV	39.30	—
Radio				
WRST	1977	1.4 GHz ($<13''$)	11.0 ± 2.0	[56]
VLA-A	1984	1.4 GHz ($1.95'' \times 1.35''$)	4.86 ± 0.59	[56]
VLA-A	1991	8.4 GHz ($0.38'' \times 0.38''$)	3.67 ± 0.14	[56]
MERLIN	1995	4.9 GHz ($0.33'' \times 0.25''$)	4.23 ± 0.31	[56]
VLA-A	1998	8.4 GHz ($0.33'' \times 0.23''$)	3.56 ± 0.10	[56]
VLA-B	2002	1.4 GHz ($6.4'' \times 5.4''$)	9.90 ± 0.10	[56]
VLA-A	2008	1.4 GHz ($2.35'' \times 2.05''$)	4.35 ± 0.10	[56]
VLA	2015	1.4 GHz ($1.99'' \times 1.46''$)	3.39 ± 0.11	[56]
VAST	2021	1.4 GHz ($8.89'' \times 7.74''$)	11.93	[66]
GMRT	2025	1.4 GHz ($2.39'' \times 2.23''$)	7.43 ± 0.30	[67]
Soft X-ray excess ^c				
XMM-Newton	2002	0.3–2 keV	4.27	[63]
XMM-Newton	2004	0.3–2 keV	3.72	[63]
Suzaku	2011	0.3–2 keV	< 1.6	[63]
Chandra	2014	0.3–2 keV	< 3.8	[58]
Swift/XRT	2016	0.3–2 keV	< 0.65	[63]
Swift/XRT	2018	0.3–2 keV	< 0.55	[63]
Swift/XRT	2020	0.3–2 keV	< 1.97	[63]
Swift/XRT	2021	0.3–2 keV	< 0.79	[63]
Swift/XRT	2024	0.3–2 keV	30.29	[38]

Notes. ^a The flux densities were derived from optical spectral fitting as elaborated in [55].

^b Measurements from IUE and HST/COS are derived from spectral fitting as elaborated in [55]. The XMM/OM and Swift/UVOT flux measurements are at the central wavelength of the UVW2, far-UV filter having a total band pass of 1600 Å–3500 Å for UVOT and 1800 Å–3250Å for OM.

^c Integrated fluxes in the quoted energy range.

^d UV/optical fluxes are in units of 10^{-16} erg s $^{-1}$ cm $^{-2}$ Å $^{-1}$; X-ray fluxes in 10^{-12} erg s $^{-1}$ cm $^{-2}$; Radio flux densities in mJy. Optical, UV and radio continuum fluxes are in rest-frame wavelength.

^e † denotes data retrieved from the XMM-Newton upper limit server. ‘–’ denotes measurement derived from this work.

B Bolometric luminosity

B.1 Methods of estimating bolometric luminosity

Here we discuss the different methods typically used for estimating the bolometric luminosity and in the subsequent section, we discuss its impact on the $\alpha_{\text{ox}} - \lambda_{\text{Edd}}$ relation. Two of the most widely used methods rely on empirical correlations: one uses the $\alpha_{\text{ox}} - L_{\text{2500\AA}}$ linear relation and the other estimates bolometric luminosity from the 2–10 keV integrated X-ray luminosity, both drawn from large samples of bright Seyferts. In the first method, a linear relationship between L_{2keV} and $L_{\text{2500\AA}}$ is constrained after SED modeling of 545 un-obsured, radio-quiet Type 1 AGNs from the XMM-COSMOS survey, spanning a $z \sim 0.04 - 4.25$ and four orders of magnitude in L_{bol} . From Eq. 11 of [21], the derived relation between L_{bol} and α_{ox} is given as:

$$\log(L_{\text{bol}}) = \log(L_{\text{2-10 keV}}) + 1.561 - 1.853 \alpha_{\text{ox}} + 1.226 \alpha_{\text{ox}}^2. \quad (5)$$

In the second method [86], the bolometric correction factor K_{bol} is based solely on the hard X-ray fluxes, derived empirically for a sample of 1000 bright, X-ray selected Type 1 and Type 2 AGNs. Their final sample spans $z \sim 0 - 4$ and four orders of magnitude in L_{bol} . We applied the Eq. 3 from [86] based on the 2–10 keV X-ray luminosity (L_X):

$$K_{\text{bol}}(L_X) = a \left[1 + \left(\frac{\log(L_{\text{2-10 keV}}/L_{\odot})}{b} \right)^c \right], \quad (6)$$

where the values of a , b , c are determined empirically as 15.33 ± 0.06 , 11.48 ± 0.01 and 16.20 ± 0.16 , respectively and L_{\odot} is the Solar luminosity equaled 3.83×10^{33} ergs s^{-1} . The final expression for L_{bol} along with its propagated uncertainty is :

$$L_{\text{bol}} = K_{\text{bol}} \times L_{\text{Edd}} \quad (7)$$

and,

$$\begin{aligned} \left(\frac{\sigma_{L_{\text{bol}}}}{L_{\text{bol}}} \right)^2 &= \left(\frac{\sigma_a}{a} \right)^2 + \left(\frac{cy}{b(1+y)} \right)^2 \sigma_b^2 + \left(\frac{y}{1+y} \ln \left(\frac{x}{b} \right) \right)^2 \sigma_c^2 \\ &+ \left(\frac{cy}{x(1+y) \ln 10} \right)^2 \left(\frac{\sigma_{L_X}}{L_X} \right)^2 + \left(\frac{\sigma_{M_{\text{BH}}}}{M_{\text{BH}}} \right)^2, \end{aligned} \quad (8)$$

where,

$$x \equiv \log \left(\frac{L_X}{L_{\odot}} \right), \quad y \equiv \left(\frac{x}{b} \right)^c, \quad K_{\text{bol}} = a(1+y). \quad (9)$$

In our work, we employ the SED integration method based on straightforward spectral fitting made with XSPEC software, and integration of the whole flux over the observed wave band. For each epoch with contemporaneous Swift XRT and UVOT coverage, we constructed a broadband SED and modeled it in three components.

First, to estimate the integrated UVOT flux at each epoch, we modeled the host-subtracted UVOT SED with a powerlaw in wavelength space, $F_{\lambda} = A \lambda^{\alpha}$, fitted in log–log space using **weighted linear regression**, where the uncertainty in $\ln F_{\lambda}$ was taken as $\sigma_{\ln F} = \sigma_F/F$. The best-fit model was then analytically integrated over the wavelength interval spanned by the available UVOT bands for that epoch, $[\lambda_{\text{min}}, \lambda_{\text{max}}]$, to obtain the integrated flux, $F_{\text{int}} = \int_{\lambda_{\text{min}}}^{\lambda_{\text{max}}} F_{\lambda} d\lambda$. Uncertainties were propagated via Monte Carlo resampling: for each epoch, we generated 5000 realizations by drawing flux densities at each wavelength from Gaussian distributions defined by their measured uncertainties, refitted the powerlaw model, and reintegrated it over the same wavelength range. We use the median integrated flux and a 1σ uncertainty derived from the 16th-84th percentile range of the resulting Monte Carlo distribution.

Second, a powerlaw model was used to interpolate between the UVW2 band and 0.3 keV, providing an estimate of the extreme-UV contribution. The resulting spectral component was then integrated over the relevant energy range, and the corresponding flux and associated uncertainties are derived following the same procedure described above. Finally, the 0.3-10 keV X-ray spectrum was modeled with an absorbed powerlaw using XSPEC, incorporating Galactic absorption using the `Tbabs` model [109]. We adopted a total hydrogen column density of $N_{\text{H}} = 2.77 \times 10^{20} \text{ cm}^{-2}$ [63]. No additional intrinsic absorption component was statistically required, supporting the classification of Mkn 590 as a ‘bare’ AGN [72]. The best fit model was extrapolated to 50 keV and using the `flux` command, the integrated X-ray flux was derived. All three fluxes have been added with errors in quadrature and converted to luminosity, which actually corresponds to observed L_{bol} .

B.2 The impact of the L_{bol} determination on the $\alpha_{\text{ox}} - \lambda_{\text{Edd}}$ relation

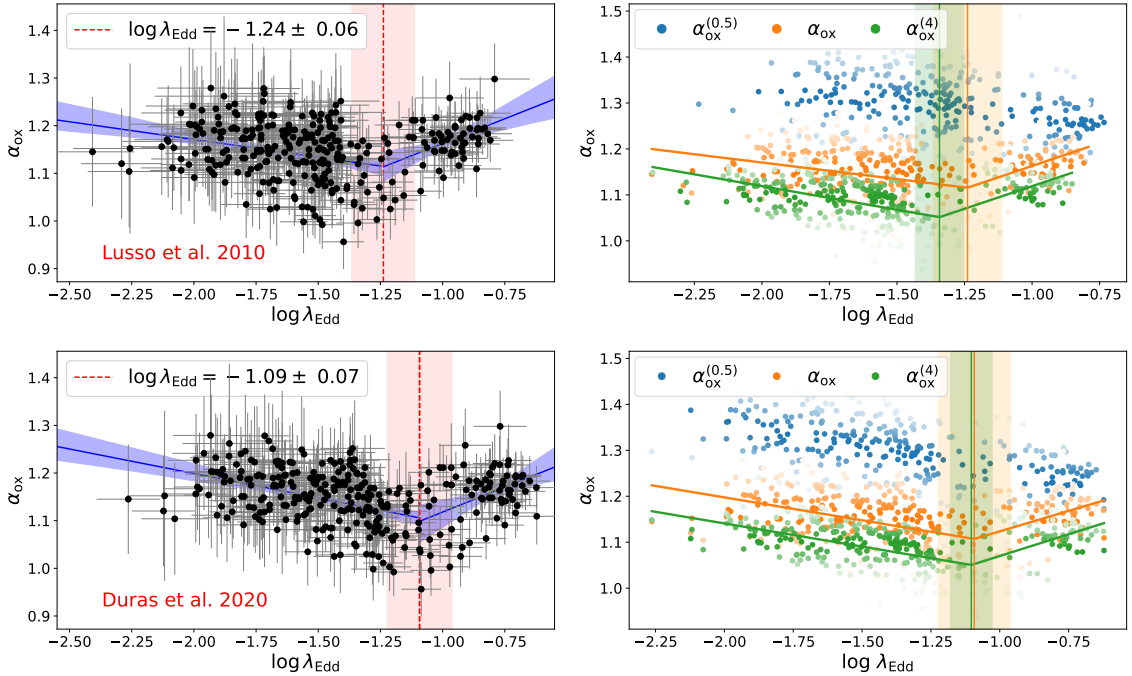


Fig. 7 From left to right, this shows the $\alpha_{\text{ox}} - \lambda_{\text{Edd}}$ relation for two distinct methods of bolometric correction factor as discussed in Appendix B.1. Statistical tools used remain the same as discussed in Sec. 4 and Appendix C.

As shown in the left panel of Fig. 7, the first two prescriptions mentioned in Appendix B.1 result in different values of break point, at $\log \lambda_{\text{Edd}} = -1.23 \pm 0.06$ and $\log \lambda_{\text{Edd}} = -1.09 \pm 0.07$ respectively. While these breakpoints are mutually consistent within their 1-sigma errors, they both are significantly higher than that obtained when using the SED integration method for the λ_{Edd} estimate, as can be seen in Fig. 2 in the main text. The impact of adopting these different L_{bol} estimates on the non-standard α_{ox} definitions introduced in Sec. 3 is shown in the right panel of Fig. 7. Thus, the inferred break point(s) is strongly method dependent.

The systematic differences between the SED-integrated luminosities and the two alternative prescriptions are quantified against a 1:1 relation in Fig. 8. Relative to the SED-based values, the [21] and [86] methods overestimate λ_{Edd} by a mean offset factor ($\langle \Delta \rangle$) of approximately 2.2 and 3.2 (in linear scaling), respectively. These average offsets are statistically significant at the $4.5\sigma - 5\sigma$ level, as judged by the statistical spread ($1\sigma = 0.08$ dex and 0.095 dex, respectively) in this offset. These overestimated L_{bol} values explain the upward shift in the inferred break point when those prescriptions are adopted.

The fact that the data points trace a curved path in these diagrams show that the SEDs (that of Mkn 590, the population average, or both) are not constant as a function of luminosity. This comparison emphasizes that dramatically variable AGN, like Mkn 590, do not behave quite like population-typical Type-1 AGN and therefore it is important to measure L_{bol} directly from the

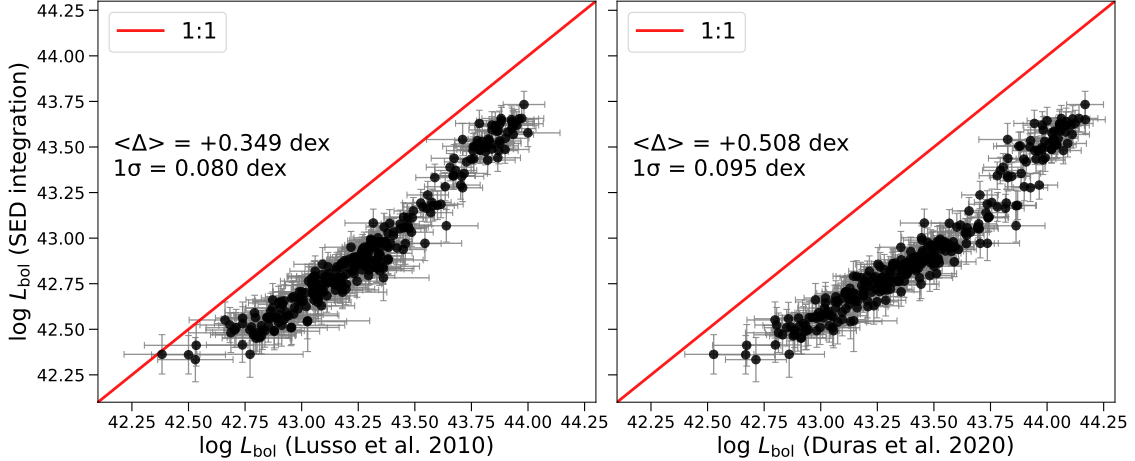


Fig. 8 Comparison between bolometric luminosities derived from SED integration method against the two alternate prescriptions described in Sec. B.1. The mean offset factor $\langle \Delta \rangle$ and its 1σ scatter are explicitly annotated.

observed data when available. This adds additional support to our choice of adopting the L_{bol} value measured directly on the *Swift* SED for our analysis.

It is important to emphasize that the bolometric correction relations of [21] and [86] are carefully calibrated using large samples of X-ray selected, persistently bright AGN. While based on a statistically large database of high-quality, carefully selected data the method carries two characteristic traits to be aware of. Firstly, the nature of determining an average bolometric correction factor (eqn. 6) or a prescription based on a fit to data with object-to-object scatter (eqn. 5) inherently assumes that the intrinsic SED of the object is very similar to that of the population average. Secondly, the population average SED and prescription will depend on the sample selection. The methods by [21] and [86] are based on X-ray bright, commonly observed Type 1 AGN that are generally not highly variable, as observed for CLAGN.

In contrast, as demonstrated in this work, Mkn 590 likely has a non-standard SED (Fig. 8) and, on top, Mkn 590 has undergone dramatic changes in both X-ray and optical/UV luminosity, reflecting substantial restructuring of its inner accretion flow. These transitions can potentially alter the thermal balance between disk and corona emission on timescales much shorter than the averaging timescales used in population studies [110, 111]. Consequently, bolometric corrections derived from narrow band luminosities may not accurately capture the instantaneous accretion power of a source undergoing rapid state changes. Furthermore, recent variability studies further show that CLAGNs exhibit flux evolution patterns that are distinct from typical Seyfert 1/2 AGN [112, 113], reinforcing the need for source specific estimates of L_{bol} . They provide a more physically representative estimate of the L_{bol} for CLAGNs, where disk-corona coupling evolves dynamically and cannot be reliably captured by static bolometric correction factors.

In conclusion, for the reasons outlined above, we compute L_{bol} by directly integrating the intrinsic broadband SED for each simultaneous *Swift*-XRT and UVOT measurements, and use it for all scientific interpretations in this work.

C Statistical tools used in this paper

To determine the turnover of the $\alpha_{\text{ox}} - \lambda_{\text{Edd}}$ relation we use **Piecewise linear regression**, also known as break point analysis or segmented regression. The tool is useful for investigating data that exhibit one or more changes in gradient. The **piecewise-regression** Python package implements this methodology by fitting continuous piecewise linear models in which both the break point locations and the segment slopes are estimated simultaneously. The approach follows the iterative algorithm of [114, 115], in which the non-linear model is linearized about initial break point estimates and refitted using ordinary least squares regression until convergence. The package further provides a comprehensive statistical framework, including confidence intervals for all model parameters and formal hypothesis testing for the presence of breakpoints. It incorporates extensive bootstrapping across many random realizations to ensure convergence toward the global minimum solution [116]. Finally, it uses the Davies test to estimate the probability of existence of at least one break point against the null hypothesis of no break point(s) [117].

We also implemented the **Deming regression** to fit linear models to either side of the break in $\alpha_{\text{ox}} - \lambda_{\text{Edd}}$ relation. The **Deming regression** is an errors-in-variables regression method that accounts for measurement uncertainties in both the dependent and independent variables [118]. It works by fitting a straight line and minimizing the squared orthogonal distances between the data points and the model, rather than the vertical residuals, while explicitly accounting for measurement uncertainties in both variables through their variance ratio. To estimate the uncertainty in fitted slope and intercept and determine the 95% confidence interval, we generated 5000 bootstrap resamplings of the dataset and refitted each realization, from which we derived the corresponding 95% confidence intervals.